Univerzita Karlova v Praze

Matematicko-fyzikální fakulta

BAKALÁŘSKÁ PRÁCE

Markéta Pešková

Studium procesu Drell-Yan v experimentu Compass s využitím polarizovaného terče

Katedra fyziky nízkých teplot

Vedoucí bakalářské práce: M.Sc. Michael Finger, CSc.

Studijní program: Fyzika

Studijní obor: Obecná fyzika

Praha 2015

Charles University in Prague

Faculty of Mathematics and Physics

BACHELOR THESIS
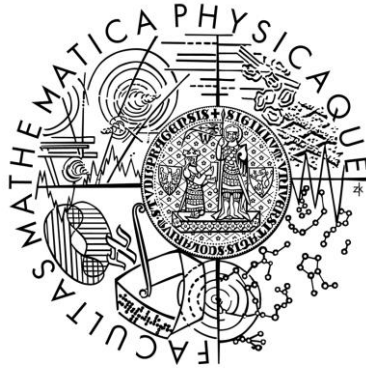
Markéta Pešková

Studies of Drell-Yan process with polarized target at COMPASS

Department of Low Temperature Physics

Supervisor of the bachelor thesis: M.Sc. Michael Finger, CSc.

Study programme: Physics

Specialization: General physics

Prague 2015

Název práce: Studium procesu Drell-Yan v experimentu Compass s využitím polarizovaného terče

Autor: Markéta Pešková

Katedra / Ústav: Katedra fyziky nízkých teplot

Vedoucí bakalářské práce: M.Sc. Michael Finger, CSc.

Abstrakt: Tato práce se snaží poskytnout úvod do studií spinové struktury nukleonu. Poznání struktury nukleonu se za posledních několik desetiletí prohloubilo, ale jeho spinová struktura je stále záhadou. Polarizovaný Drell-Yan proces je jedním z konceptů, které by mohly pomoci vyřešit otázku spinu nukleonu. Měřením spinových asymetrií v tomto procesu můžeme určit spinově závislé strukturní funkce nukleonu. Následující text obsahuje úvod do teorie semi-inklusivního hlubokého nepružného rozptylu a Drell-Yan procesu. Popisuje partonové distribuční funkce (PDF) a PDF související s příčným momentem hybnosti partonů (TMD). Dále je stručně popsán způsob, jak lze pomocí Drell-Yanova procesu nalézt TMD, což je cílem Drell-Yan programu na experimentu COMPASS s použitím transverzálně polarizovaného terče a pionového svazku v letech 2014 a 2015. Práce dále popisuje spektrometr COMPASS a systém sběru a zpracování dat. Předkládáme podmínky měření při testovacím runu Drell-Yan programu v roce 2009 a při pilotním runu v roce 2014. Z těchto dat jsme zanalyzovali produkci mionového páru a kinematické distribuce. Srovnali jsme výsledky z těchto analýz a jejich souhlas s oficiálními výsledky. A na závěr předkládáme stručný výhled na budoucí run 2015.

Klíčová slova: Drell-Yan proces, nízkoteplotní polarizovaný terč, spinová struktura nukleonu, PDFs, TMDs

Title: Studies of Drell-Yan process with polarized target at COMPASS

Author: Markéta Pešková

Department / Institute: Department of Low Temperature Physics

Supervisor of the bachelor thesis: M.Sc. Michael Finger, CSc.

Abstract: The presented thesis intends to give an introduction into the studies of the spin structure of a nucleon. The knowledge about the structure of nucleon has grown in the last few decades; however, its spin structure is still a mystery. One of the concepts that might help solving this spin puzzle is the polarized Drell-Yan process. This process can give us the access to the spin-dependent structure functions of a nucleon via measuring spin asymmetries. In the following text, an outline of the theoretical background of the semi-inclusive Deep Inelastic Scattering and the Drell-Yan is given. The Parton Distribution Functions (PDFs) and the transverse-momentum-dependent PDFs (TMDs) are discussed. And the way of accessing the TMDs via polarized Drell-Yan process is briefly described. This is the goal of the Drell-Yan program at COMPASS experiment, using the transversely polarized target and pion beam in 2014-15. The description of experimental apparatus is given and the system of collecting and processing data is outlined. The data-taking conditions of the 2009 DY beam test and the 2014 DY data-taking are presented. From the data of these runs, we performed the analysis of the dimuon pair production and the kinematic distributions. The comparison of the results from the particular run and with the official results is given. The expectations of the 2015 DY run are also discussed.

Keywords: Drell-Yan process, low-temperature polarized target, spin structure of nucleon, PDFs, TMDs

Contents

Introduction

In the last century science has profoundly expanded our knowledge about microcosm. We moved from using optical instruments to exploring more and more details about structure of matter with microscopic probes, by scattering experiments. From the well-known Rutherford's experiment which led to the discovery of the atomic nucleus, followed by finding nucleons: proton, and neutron, respectively, in the beginning of the 20th century, to studying the structure of hadrons and their constituents which continues to the present days. The capability to explore the infinitely small has grown, as the resolution was improving by reaching increasing energies in particle accelerators. The scattering experiments of R. Hofstadter from the 50's implied the existence of the internal structure of a proton. Shortly after that, Gellman and Zweig created so-called Quark Model which stated quarks as the constituents of the nucleon. The constituents of nucleon were then described by the Feynman's Parton Model as partons (1969) and then identified with the Gellman-Zweig's quarks [4]. In the 70's, the Quantum Chromodynamics (QCD) was developed and approved as the theory of the strong interaction. QCD is still being approved experimentally as a successful theory in describing various properties of hadrons and their interaction. However, this theory works fine in high energies (higher than 1 GeV[1]) where its perturbative regime is sufficient, but in a low energy (non-perturbative regime), despite of wealth of the experimental data collected on this matter, there is still much uncertainty.

One of the issues, the theory faces, is spin structure of a proton. In 1988 the European Muon Collaboration (EMC) discovered very surprising fact contradictory with contemporary knowledge that quarks contribute only one third to the total spin of a nucleon (for results see [1]). The consequent spin crisis led to creation of new theoretical tools for determining the spin structure of the nucleon. While the spin-independent nucleon structure can be described by spin-averaged structure functions and resulting parton distribution functions (PDFs), the spin structure of the nucleon can be described at Leading Order QCD by three PDFs f_1, g_1, and h_1 for each parton species, and when taking into account the transverse momentum of the quarks, it can be described by eight Transverse Momentum

---

[1] In the whole text the natural units (c = ħ = 1) are used, unless stated otherwise.

Dependent Parton Distribution Functions (TMDs[2]) which are spin and transverse momentum dependent. Most of them are still little known or completely unknown and wait to be obtained by the experiment. While PDFs can be accessed by Deep Inelastic Scattering (DIS), the effects of intrinsic transverse parton momenta which are described by TMDs can be measured e.g. by two approaches, complementary to each other: Semi-Inclusive Deep Inelastic Scattering (SIDIS), or Drell-Yan process (DY). One of the various experiments where these processes are studied is "COmmon Muon and Proton Apparatus for Structure and Spectroscopy" (COMPASS; [2]) in CERN.

Purpose of this thesis is to provide a brief review of the theoretical background of Parton model, PDFs and TMDs, Drell-Yan process, and SIDIS in comparison to that. Then we will give a short description of COMPASS apparatus and then we will take a view on the experimental efforts in COMPASS DY program and make a basic analysis of the 2009 and 2014 data.

---

[2] TMDs describe correlations between the spin of hadron and spins and momenta of partons

1. Physics of the Drell-Yan process

1.1. Deep inelastic scattering

Most experiments probing microscopic structure of matter are based on scattering particles on other particles. Elastic scattering is a collision of incident particle on a target particle where both particles remain unchanged, there are no energy losses and no new particles are created. By this process the size, shape or distribution of charge of nuclei can be measured. Inelastic scattering enables the probe to penetrate to subnuclear sizes and explore the intrinsic structure of the nucleus or nucleon. Inelastic scattering occurs when the incoming particle transfers a part of its energy to the target particle or its constituent and it becomes excited or breaks up and new particles are born [3]. In this section we will shortly describe the process of deep inelastic scattering which was important in the formulation of the parton model.

Let us now introduce the kinematics of the special case of this process, scattering leptons on hadrons (more information about DIS is available in [4]), described by:

$$l(k) + H(P) \rightarrow l'(k') + X, \tag{1.1}$$

where X denotes any outgoing hadrons created from the transfer of energy of the incoming lepton, l and l' are incoming and scattered lepton, respectively, H is the target hadron, and letters in the parenthesis correspond to four-momenta of the corresponding particles. If X is the initial hadron, then (1.1) describes an elastic scattering, this process is shown on the figure 1.1a which represents the lowest order Feynman diagram of electron-proton collision.

(a)   Elastic scattering on pointlike proton   (b)   Inelastic scattering
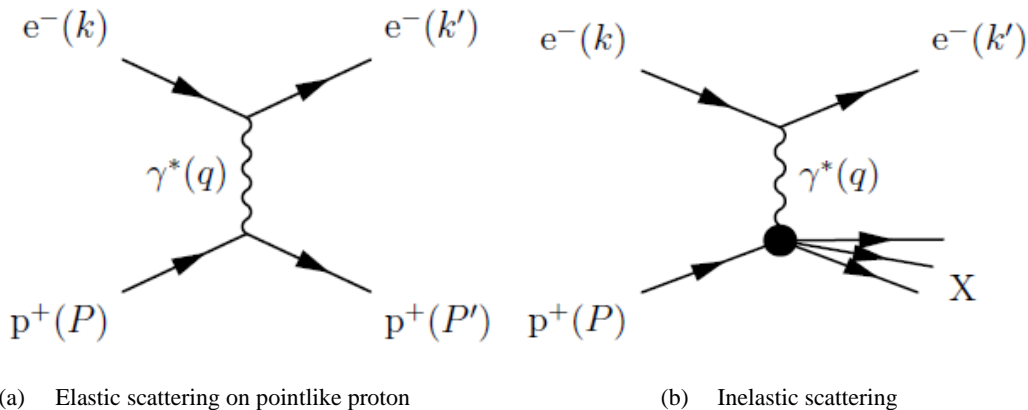
Figure 1.1: The lowest order Feynman diagrams of electron-proton scattering [5].

The interaction is mediated either by photon or Z boson in case that $l = l'$, or charged $W^{\pm}$ boson when the leptons differ at one unit of charge (for example when the scattering lepton

is neutrino) however the last process is not our concern. Following relativistic invariants are usually used for describing the inelastic scattering:

$$s \equiv (k+P)^2 = M^2 + 2kP = M_p(2E_{lab} + M_p), \qquad (1.2)$$

$$Q^2 \equiv -q^2 = -(k-k')^2 = 2kk' = 2EE'\sin^2(\vartheta/2), \qquad (1.3)$$

$$x \equiv \frac{Q^2}{2Pq} = \frac{Q^2}{2M_p\upsilon} = \frac{Q^2}{Q^2 + W^2 - M_p^2}, \qquad (1.4)$$

$$y \equiv \frac{qP}{kP} = \frac{E_{lab} - E'_{lab}}{E_{lab}} = \frac{\upsilon}{E_{lab}} = \left(\frac{s - M_p^2}{s}\right)\frac{1 - \cos\vartheta*}{2}, \qquad (1.5)$$

$$W^2 \equiv (q+P)^2 = \frac{Q^2(1-x)}{x} + M_p^2, \qquad (1.6)$$

where W is the invariant mass of the hadronic system X, the Mandelstam invariant s describes the initial state and also has a meaning as total CMS (center-of-mass) energy squared. The M_p variable corresponds to proton mass, E and E' are the energies of incoming and scattered lepton in the CMS, respectively, P and k, k' describe the four-momenta of hadron and lepton, and ϑ stands for the angle of the scattered lepton. Invariant Q^2 is a square of the transferred four-momentum, The x is called Bjorken's x and it characterizes the inelasticity of the collision and for the elastic case it equals 1. The term "deep inelastic scattering" means that the kinematic domain is $Q^2 \gg M_p$ and $P.q \gg M_p$ (see [4]).

The following is an overall description of elastic and inelastic scattering cross-section. In quantum electrodynamics the cross-section for the elastic scattering of electron on a point-like proton can be derived (more details in [4]):

$$\frac{d\sigma}{dQ^2} = \frac{4\pi\alpha^2}{Q^4}\left(1 - y + \frac{y^2}{2} - \frac{M^2 y}{2kP}\right). \qquad (1.7)$$

In the laboratory frame the formula is given:

$$\frac{d\sigma}{dQ^2} = \sigma_{Mott}\frac{E'_{lab}}{E_{lab}}\left[1 + \frac{Q^2}{2M^2}\tan^2\left(\frac{\vartheta_{lab}}{2}\right)\right], \quad \sigma_{Mott} = \frac{\alpha^2\cos^2(\vartheta_{lab}/2)}{4E_{lab}^2\sin^4(\vartheta_{lab}/2)}. \qquad (1.8)$$

Where σ_{Mott} is the Mott formula for scattering of relativistic Dirac particle (unpolarized) on static point-like charge potential, and α is fine structure constant. If we consider the internal structure of a proton, it can be described by the so-called form-factors[3] or

---

[3] Form-factor $F(q^2)$ is a Fourier transformation of charge distribution in a particle and in the scattering cross-section formula it accounts for the effect of the extension of the charge distribution in a nonpoint-like particle [3].

distribution functions (more can be find e.g. in [6]). We will return to the subject of distribution functions in more detail in Chapter 1.2 and 1.3.

For derivation of the cross-section for inelastic scattering we have to consider that the energy is not conserved in the process and thus variables Q^2 and v become independent and it leads to the following formula [4]:

$$\frac{d\sigma}{dxdQ^2} = \frac{4\pi\alpha^2}{Q^4}\left[\left(1 - y - \frac{M^2xy}{s}\right)\frac{F_2(x,Q^2)}{x} + y^2F_1(x,Q^2)\right]. \qquad (1.9)$$

Where F_1 (x,Q^2) and F_2 (x,Q^2) are called inelastic electromagnetic form-factors or structure functions of the proton. Structure functions are related to the Parton Distribution Functions (PDFs) which will be discussed later.

1.2 Parton Model, Quarks and QCD

The first experiment that measured structure functions and elastic form-factors of the proton was at the SLAC laboratory (Standford Linear Accelerator) using electron beam. The experiment showed that the elastic form-factors rapidly decrease with rising Q^2 and conversely inelastic form-factors increase to a constant non-zero value. This can be explained that if the target nucleon has an internal structure then it is less probable that its constituents recombine back after the collision in high energies. The behavior of inelastic form-factors in high energies had been predicted by Bjorken and it is called Bjorken scaling [4]. But later it has been shown that the structure functions actually do approach zero instead, even if it's very slow, thus it is called approximate scaling.

The interpretation of the results of SLAC experiment was first given by R. P. Feynman and it led to the formulation of the parton model[4]. Feynman stated that DIS can be modeled as "quasi-free scattering from point-like constituents within the proton, as viewed from a frame where proton has infinite momentum." [8]

In the infinite momentum frame the proton becomes Lorentz-contracted to a disc and the internal movement of the partons is strongly slowed down by the time dilatation, so the constituents can be considered as free particles during the collision. The hadronization process, which is a conversion of the partons to the final state hadrons, takes place much later than the e-p collision itself, as is shown on the figure 1.2. Transverse momentum of the partons can be neglected (This is called collinear approximation) as well as their rest masses

---

[4] Parton is an abbreviation for "part of proton" [7]

and only their longitudinal momentum plays a role. The momentum of the i-th parton can be expressed as a fraction of the proton momentum $\eta_i P$. Note that the momentum conservation law of the lower vertex in figure 1.1a:

$$\left(\eta_i P'\right)^2 = \left(\eta_i P\right)^2 - Q^2 + 2\eta_i Pq \Rightarrow Q^2 = 2\eta_i Pq , \qquad (1.10)$$

implies that x variable from (1.4) represents the fraction of the proton momentum η_i carried by a particular parton. Now we can use the description of the scattering electrons from partons inside the proton to calculate the cross-section of inclusive e-p scattering which depends on kinematic variables of the scattered electron only. This cross-section is a sum of cross-sections of scattering on the individual charged partons. Under the consideration of $s \rightarrow \infty$ in (1.9), and thus the y variable being small, the elastic cross-section on parton with charge fraction e_p is given:

$$\frac{d\sigma}{dQ^2} = \frac{4\pi\alpha^2 e_p^2}{Q^4} . \qquad (1.11)$$

After comparing (1.9) with weighted sum of the partonic cross-sections, we get the inelastic electron-proton cross-section:

$$\frac{d\sigma}{dxdQ^2} = \frac{4\pi\alpha^2}{Q^4} \frac{F_2\left(x,Q^2\right)}{x} = \frac{4\pi\alpha^2}{Q^4} \sum_i e_i^2 f_i\left(x\right), \qquad (1.12)$$

where $f_i(x)$ is the probability to find the i-th parton with charge e_i and momentum fraction xP inside the proton. The functions $f_i(x)$ are called the Parton Distribution Functions (PDFs).
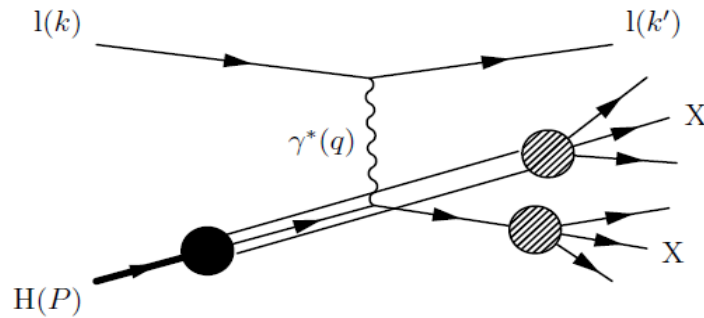
Figure 1.2: Deep inelastic scattering in parton model. The process of hadronization takes place after the collision, so-called independent fragmentation model (taken from [5]).

The function $F_2(x,Q^2)$ can be expressed as follows:

$$F_2\left(x,Q^2\right) = F_2\left(x\right) = x\sum_i e_i^2 f_i\left(x\right). \qquad (1.13)$$

We can see that the parton model naturally leads to Bjorken scaling i.e. F_2 does not depend on Q^2. The function $F_1(x,Q^2)$ from the cross-section (1.9) also plays a role within

low energies. It can be approximated by the Callan-Gross relation for partons with ½ spin: $F_2(x,Q^2) = 2xF_1(x,Q^2)$ which has been confirmed by experimental data, e.g. [4].

The next natural step would be the identification of partons as quarks from the additive quark model but then some difficulties arise. The first of them lies in a clear evidence that there must be some other constituents of proton not answering to electromagnetic or weak probes, thus without any charge. The so-called momentum sum rule, defined as follows:

$$\sum_i \int_0^1 x f_i(x) dx = 1,\tag{1.14}$$

was not satisfied with the measurement as the actually measured value is only 0,5 [6]. It was suggested that there must be some particles "gluing" the quarks together, and that would be carrying the rest of total momentum.

Another problem emerges again if we try to interpret partons as quarks. As only quarks u, d, c, and s can be constituents of the proton (while b and t are too heavy) the proton structure function can be calculated as a sum of the PDFs of all quarks and antiquarks:

$$F_2^p = x\left(\frac{4}{9}\left[f_u(x) + \bar{f}_u(x) + f_c(x) + \bar{f}_c(x)\right] + \frac{1}{9}\left[f_d(x) + \bar{f}_d(x) + f_s(x) + \bar{f}_s(x)\right]\right).\tag{1.15}$$

Integrating $F_2(x)$ over x we get a mean square charge per parton. The experimentally measured value is $0,17 \pm 0,009$ [4] which is considerably lower than expected value of ⅓ of the 3-quark model. So this also points at possible existence of non-charged constituents of proton.

And the last of the issues is the behavior of the parton distribution which is roughly proportional to 1/x for x → 0 and integral from this function diverges. This would indicate that there is infinite number of charged partons in the proton. If we define so-called valence and sea functions as a combination of quark and antiquark distribution functions as follows:

$$f_q^{val}(x) \equiv f_q(x) - \bar{f}_q(x), \quad f_q^{sea}(x) \equiv \bar{f}_q(x),\tag{1.16}$$

And if we integrate the valence function for u and d quark, we get the result fully in agreement with static quark model [4]:

$$\int_0^1 f_u^{val}(x)dx \approx 2 \quad \int_0^1 f_d^{val}(x)dx \approx 1\tag{1.17}$$

These problems led to the formulation of the non-abelian gauge theory of strong interaction, the Quantum Chromodynamics (QCD) which solved them. It is based on SU(3)

symmetry of color charges with eight massless and colored field quanta, vector bosons called gluons [6]. There are three color charges named after three basic colors: R, G and B, and three corresponding anticharges. In contrast to Quantum Electrodynamics (QED), where mediating bosons (photons) do not interact, gluons carry the color charge which allows them to interact with each other (see Feynman diagrams of the figure 1.3)


(a) (b)
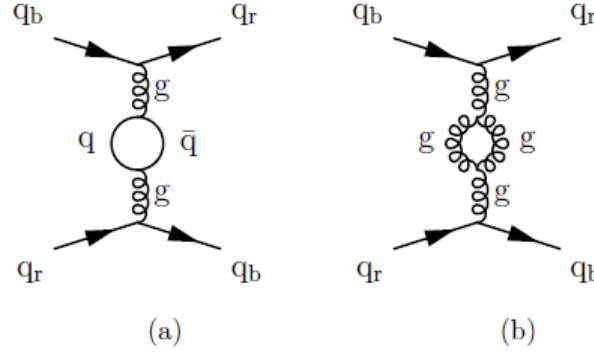
Figure 1.3: The second nontrivial order of quark-quark interaction where (a) is virtual quark and (b) gluon loops [5].

Another attribute of the QCD is phenomenon called asymptotic freedom discovered by Politzer, Gross and Wilczek which denotes the behavior of the interaction with respect to energy and distance. In the limit of infinite energy (equivalent to distances going to zero) quarks appear to be free [4]. On the other hand, quarks cannot get outside of a hadron and in low energies (less than 1 GeV) the coupling (represented by the coupling constant α) is so strong that it cannot be treated by perturbative method and leads to so-called confinement, i.e. there are no free quarks. The consequence of this is that the low energy properties of hadrons cannot be computed by perturbative QCD.

The hadronization process can be described by the Fragmentation functions which denote the probability that the produced hadron has a given fraction of energy and transverse momentum with respect to the original parton.

Now we shortly summarize the problematics: A nucleon consists of three valence quarks described by the $f_q^{val}(x)$ distribution functions. The quarks are held together by a potential that is created by a complicated multi-gluon exchange. In that exchange a virtual pair quark-antiquark is born as depicted on figure 1.3a. As these particles are virtual, they have to recombine eventually but their "virtuality" is small in comparison to $\sqrt{Q^2}$ of proton-electron collision, so they can live long enough to have an electron scattered on them as on the valence quarks [4], distribution of these virtual pairs is described by the $f_q^{sea}(x)$ functions.

1.3 Transverse-spin-dependent structure functions

1.3.1 The nucleon spin structure

The structure of nucleons has been studied by the deep inelastic scattering of charged leptons or neutrinos and these experiments elucidated well the quark-gluon structure of nucleon. However, the distribution of the spin of the nucleon among its constituents is still barely known. This knowledge can be derived from the experiments using DIS of polarized leptons on polarized targets [1]. One such experiment was carried out at SLAC using polarized electron beam or on several SPS[5] experiments at CERN using high energy muon beam which will be discussed in following chapters.

The nucleon is a spin ½ particle. Its spin is composed of following parts [9]:

$$\frac{1}{2} = \frac{1}{2}\Delta\Sigma + \Delta G + L_q + L_g \, , \qquad (1.18)$$

which are the contributions of its constituents being $\Delta\Sigma$ the total number of quarks with spin parallel to the spin of the nucleon minus the number of quarks with anti-parallel spin; once weighted by the spin of the quark $^1/_2$, this is the total contribution of quarks to spin of the nucleon; ΔG is the contribution from the spin of the gluons; and L_q and L_g denote the contributions of the orbital momentum of the quarks and gluons, respectively.

In the simplest case, taken in account three quarks only, the quark spin contribution is given by two valence quarks with parallel spin and one with anti-parallel, ½ + ½ - ½ = ½ hence the $\Delta\Sigma$ equals 1 and all the other distributions are zero. We can also have e.g. 3 quarks with spin parallel and a gluon with spin antiparallel, then it gives $\Delta\Sigma = 3$ and $\Delta g = -1$ [9]. QM in a non-relativistic mode corresponds with the first simplest case above. If we include the relativistic corrections to the QM, we get $\Delta\Sigma \approx 0.75$, $L_q \approx 0.125$ and $\Delta g = L_g = 0$ (ibid.). It's not possible to compute $\Delta\Sigma$ within QCD as this is a low-energy quantity, but we can decompose it from the contribution of the quark flavors that can be found in nucleon, $\Delta\Sigma = \Delta u + \Delta d + \Delta s$, and additionally we can neglect Δs as the strange contribution in a nucleon is known to be generally small. It was shown that this quark distribution is $\Delta\Sigma \approx 0.6$. The problem came with the EMC experiment measurement carried out in 1988. This experiment measured spin asymmetries (see lower in this section) in high energy muon proton DIS and from them extracted the quark distribution $\Delta\Sigma = 0.18 \pm 0.09 \pm 0.14$ and $\Delta s = -0.19 \pm 0.03 \pm 0.04$ [1], thus in a clear disagreement with the expected value ($\Delta\Sigma \approx 0.6$). This is referred to

---

[5] Super Proton Synchrotron

the so-called spin crisis. The spin crisis triggered large amount of new experimental and theoretical effort for finding an explanation for it. The next experiments, which aimed at measurement of the quark spin contribution, were SMC and more recently COMPASS. The COMPASS 2007 μp DIS data gave a more accurate result: $\Delta\Sigma = 0.32 \pm 0.03$ [10]. However, the question of what carries the most of the nucleon spin still hasn't been solved.

Structure of a nucleon in collinear approximation can be described by three PDFs. Apart from the $f_1(x) \equiv q(x)$ unpolarized distribution function[6] mentioned in the previous section (denoted as $f_i(x)$), there is firstly the helicity[7] distribution function $g_1{}^q(x)$ defined as follows [4]:

$$g_1^q(x) \equiv \Delta q \equiv q_{1i} \uparrow (x) - q_{1i} \downarrow (x), \tag{1.19}$$

that describes the difference between the density of quarks with spin parallel and the quarks with spin anti-parallel with respect to the longitudinally polarized hadrons. And the third PDF, is the transversity $h_1^q(x) \equiv \Delta_T q$ which is similar, but for the transversely polarized hadrons. The $g_1{}^q(x)$ can be measured using the polarized lepton beam and longitudinally polarized target, and on the other hand $h_1{}^q(x)$ requires a transversely polarized target. Although $h_1{}^q(x)$ is a leading order quantity, it is very little known [5]. The reason is that $h_1{}^q(x)$ is a chiral-odd function hence its measurement requires a flip of the probed quark chirality. However, such behavior is mostly suppressed in DIS. To measure the transversity, one has to flip the chirality twice, so either has two hadrons in initial state, as DY, or one hadron in the initial state and one in the final, like Semi-Inclusive DIS (SIDIS), both of them will be discussed briefly later. Both of the methods are complementary and each of them has its advantages.

Measuring the experimentally accessible quantities $\sigma\uparrow\uparrow$ and $\sigma\uparrow\downarrow$ which are the cross-sections of beam and target with polarization parallel and antiparallel, respectively, we can construct the asymmetry A_1:

$$A_1 = \frac{\sigma^{\uparrow\uparrow} - \sigma^{\uparrow\downarrow}}{\sigma^{\uparrow\uparrow} + \sigma^{\uparrow\downarrow}}. \tag{1.20}$$

Then, if we use QED, Parton Model, consider only high energy limit (thus neglecting the lepton mass), and using only helicity instead of the full spin four-vector, we can derive (for more, see [5]):

---

[6] The subscript 1 denotes the leading order of perturbative QCD.

[7] The helicity denotes the projection of the particle spin onto the direction of its momentum.

$$A_1(x) = \frac{\left(1 - (1 - y)^2\right)}{\left(1 + (1 - y)^2\right)} \frac{x}{F_2(x)} \sum_i e_i^2 \Delta q_i(x). \qquad (1.21)$$

As soon as we measure the $F_2(x)$ structure function and the asymmetry, we can determine the helicity function. Note that the measured asymmetry has to be modified by a correction factor $P_T P_B f$, where P_T is the target polarization, P_B denotes the beam polarization, and f is so-called dilution factor, i.e. the fraction of polarizable nuclei in the target [7] where as much precise as possible knowledge of the beam and target parameters is necessary. So, the experimentally measured spin asymmetries are related to the ideal asymmetries by following formula:

$$A_1^{\text{exp}}(x) = A_1(x) P_T P_B f, \qquad (1.22)$$

The so-called polarized structure functions for the proton $g_1^p(x)$ is given:

$$g_1^p(x) = \frac{1}{2} \sum_i e_i^2 \Delta q_i(x), \qquad (1.23)$$

and similarly for the neutron. And finally the total contribution of quark spins to the total proton and neutron spin, respectively, is given by the integrals (for more see [4]):

$$\Gamma_1^p = \int_0^1 dx\, g_1^p(x) = \frac{1}{2}\left(\frac{4}{9}\Delta(u) + \frac{1}{9}\Delta(d) + \frac{1}{9}\Delta(s)\right), \qquad (1.24)$$

$$\Gamma_1^n = \int_0^1 dx\, g_1^n(x) = \frac{1}{2}\left(\frac{4}{9}\Delta(d) + \frac{1}{9}\Delta(u) + \frac{1}{9}\Delta(s)\right). \qquad (1.25)$$

By summing (1.24) and (1.25) we get the following equation together with the results of the SMC (the predecessor of the COMPASS experiment [4]):

$$\Gamma_1^p + \Gamma_1^n = \frac{5}{18}\left(\Delta(u) + \Delta(d) + \frac{2}{5}\Delta(s)\right) = 0.073 \pm 0.03. \qquad (1.26)$$

$$\Delta(u) + \Delta(d) = 0.26 \pm 0.09, \qquad (1.27)$$

which gives the fraction of the spin of the proton carried by the u and d quarks and antiquarks.

1.3.2 Transverse Momentum Dependent structure functions

The collinear approximation cannot be applied on all the measured observations. Hence, we have to move to the spin structure of the nucleon considering the transverse momentum k_T of the particular quark. One of the approaches dealing with transverse momentum are

Transverse Momentum Dependent (TMD) PDFs[8] [2] which are applicable for small transverse momenta.

There are six time-reversal invariant TMDs: $f_1(x, k_T^2)$, $g_{1L}(x, k_T^2)$, $h_1(x, k_T^2)$, $g_{1T}(x, k_T^2)$, $h_{1T}^\perp(x, k_T^2)$, and $h_{1L}^\perp(x, k_T^2)$. The first three TMDs integrated over k_T^2 give the already discussed $f_1(x)$, $g_1(x)$, and $h_1(x)$ distributions. The later three vanish after the integration. If we don't demand the time-reversal invariance, two more T-odd[9] distributions arise. The first is called Boer-Mulders function $h_1^\perp(x, k_T^2)$ and describes the correlation between the transverse spin and transverse momentum of the quark within an unpolarized nucleon. The second is Sivers function $f_{1T}^\perp(x, k_T^2)$ and denotes the influence of the transverse spin of the nucleon on the transverse momentum of its quark. A correlation between the k_T and the transverse polarization of a parton or hadron is possible only for non-vanishing orbital angular momentum of quarks [2]. As the QCD is a T-invariant theory, those distribution functions should be equal to zero. However, experiments have shown that they have non-zero value. It is very important to determine the $f_{1T}^\perp$ and $h_1^\perp$ as well as the h_1 function to reveal more about the spin structure of hadrons.

We have used the Amsterdam notation of PDFs where letters f, g, and h denote unpolarized, longitudinally polarized, and transversely polarized structure functions, respectively. The subscript 1 means that we are using the leading-order quantity, subscripts T and L stand for the transversely or longitudinally polarized parent hadron, and superscript $\perp$ denotes transverse momenta with uncontracted Lorentz indices [5].

As we mentioned above, the transversity functions can be accessed e.g. by either DY or SIDIS. Concerning the DY program of COMPASS, which will be the focus of this thesis, the experiment concentrates mainly on the transversity, Boer-Mulders, and Sivers functions. The other possibility is SIDIS, which has also been a part of the COMPASS program. In SIDIS the chirality is conserved by the convolution of PDFs with polarized quark fragmentation functions [2]. On the contrary, the DY process has the advantage that no fragmentation function takes place as there is no hadron in the final state. As the Boer-Mulders and Sivers functions are T-odd, there is a prediction based on the TMD approach that these distributions change their sign [2]:

$$f_{1T}^\perp(DY) = -f_{1T}^\perp(SIDIS) \quad h_1^\perp(DY) = -h_1^\perp(SIDIS) \tag{1.28}$$

---

[8] Usually referred simply to TMDs.

[9] Time-reversal odd.

And this is the crucial effort of the COMPASS experiment, to test this sign change using the same spectrometer and polarized target in both DY and SIDIS experiments.

1.4 The Unpolarized Drell-Yan process

As it has been noted above, the DY process is an excellent tool to study transversity and TMD *T*-odd PDFs. In this section we will provide a short introduction of the DY formalism and observables. The choice of the reference frames and the formulation of the DY cross-section follows the article by Arnold, Metz, and Schlegel [11]. For the discovery of this process, see [12]. Firstly, we discuss the unpolarized case. We consider the hadron-hadron reaction with production of massive dilepton pair:

$$H_a(P_a) + H_b(P_b) \rightarrow l^-(k) + l^+(k') + X . \tag{1.29}$$

Where $P_{a,b}$ are momenta of the colliding hadrons, k and k' are the momenta of leptons, and $q = k + k'$ is the total momentum of the lepton pair or equivalently, of the virtual photon. The figure 1.4 shows the Feynman diagram of such a process:
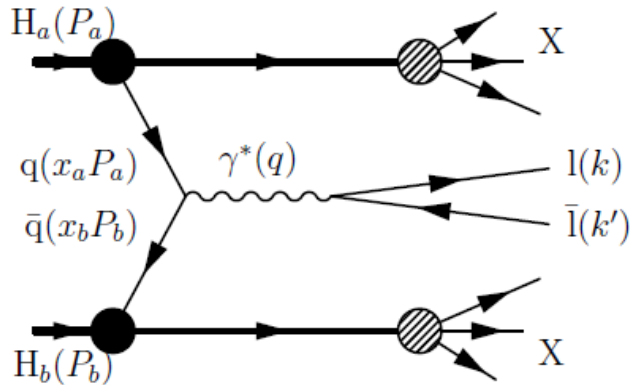

Figure 1.4: The Feynman diagram of the Drell-Yan process: annihilation of a quark-antiquark pair into a lepton pair. The filled circles denote the PDFs of the hadrons and shaded ones the independent fragmentation functions in the independent fragmentation model [5].

We assume a reference frame of hadron-hadron collision head-on along the z axis. The following invariant kinematic variables can be defined:

$$s = (P_a + P_b)^2,$$

$$x_{a,b} = \frac{q^2}{(2P_{a,b}q)},$$

$$x_F = x_a - x_b \cong \frac{2|q|}{\sqrt{s}}, \tag{1.30}$$

$$\tau = \frac{4m^2}{s},$$

$$M_{ll}^2 = Q^2 = q^2 \cong s x_a x_b,$$

where s describes the total CMS energy squared, x has the same meaning as in the formula (1.6) i.e. the momentum fraction carried by a parton from $H_{a,b}$, x_F is so-called Feynman variable (the equality applies only if we neglect the parton masses, also for the last formula), and the last is the invariant mass squared of the dilepton. We can express the cross-section of the process using the parton model as follows [4]:

$$\frac{d\sigma}{dm^2 dx_F} = \frac{1}{3}\left[\frac{4\pi\alpha^2}{3m^2}\right]\sum_i e_i^2 \iint f_{1i}(x_a)\bar{f}_{1i}(x_b)\delta(x_a x_b s - m^2)\delta(x_a - x_b - x_F)dx_a dx_b , \tag{1.31}$$

where the expression in the square brackets stands for the parton-antiparton annihilation cross-section. The factor of ⅓ reflects the probability that both quark and antiquark have the same color charge. It is present because the produced leptons are colorless. The index i runs over both quarks and antiquarks to take into account both cases that a quark is from the hadron a or b. Integration of the (1.31) produces following expression:

$$\frac{m^3 d\sigma}{dm dx_F} = \frac{8\pi\alpha^2}{9\sqrt{x_F^2 + \tau}}\left[\sum_i e_i^2 f_{1i}(x_1)\bar{f}_{1i}(x_2)\right], \quad x_{1,2} = \frac{1}{2}\left(\pm x_F + \sqrt{x_F^2 - \tau}\right) \tag{1.32}$$

The right side of the equation scales with the parameter τ independently on the PDFs (this has been verified experimentally). This is another example of scaling behavior of the parton model [12].

1.5 The Polarized Drell-Yan process

The unpolarized DY process played an important role in determining the PDFs of hadrons. DY process still attracts the attention of experimentalists and theoreticians, but recently the attention has moved to its polarized version because it allows us to study the TMDs, and some other issues both in perturbative and nonperturbative QCD. Nevertheless, the experiments with the polarized DY are rather demanding because of its low counting rate [11].

As was shortly presented in the previous section, the PDFs of the two acting hadrons are connected in convolution in DY formalism. They can be extracted by QCD-factorization

theorem (for more, see [11]) which can be applied under a condition of sufficiently large mass of produced leptons. This is one of the reasons why one usually searches for muons on the final state. This is the case of the COMPASS DY program and other future experiments, such as RHIC (2016 or later), J-PARC (after 2018), NICA (2018 or later), FAIR (2018 or later) or IHEP [5]. Additionally, as was mentioned before, the COMPASS experiment is unique because it provides also measurements of SIDIS which is complementary to DY.

In COMPASS DY program the reaction:

$$\pi^-(P_\pi) + p(P_p, S_p) \to \gamma^*(q) + X \to \mu^-(l) + \mu^+(l') + X, \qquad (1.33)$$

will be studied using negative-pion beam and transversely polarized proton target. In the (1.33) the parameter S_p is a proton spin four-vector with properties: $S_p \cdot P_p = 0$ and $S_p^2 = -1$. There are two reference frames to describe the DY process [2]: The target rest frame (TF) defined by the unit vector $\hat{z}$ along the beam momentum, $\hat{x}$ along the transverse momentum q_T of the virtual photon, and $\hat{y} = \hat{z} \times \hat{x}$, yielding:

$$P_{\pi,TF}^\mu = \left(P_{\pi,TF}^0, 0, 0, P_{\pi,TF}^3\right), \qquad (1.34)$$

$$P_{p,TF}^\mu = \left(M_p, 0, 0, 0\right), \qquad (1.35)$$

$$q_{TF}^\mu = \left(q_{TF}^0, 0, 0, q_{TF}^3\right), \qquad (1.36)$$

$$S_{TF}^\mu = \left(0, S_T \cos\phi_S, S_T \sin\phi_S, S_L\right), \qquad (1.37)$$

Where Φ_S is the angle between the transverse components of spin (with respect to $\hat{z}$) and virtual photon momentum (see figure 1.5a). The second frame is the Collins-Soper frame (CS) as the rest frame of the virtual photon. It can be obtained from the TF by boosting along the photon momentum. When we neglect the muon mass, we can write the muon and antimuon momenta as follows [2]:

$$l_{CS} = \frac{q}{2}\left(1, \sin\theta\cos\phi, \sin\theta\sin\phi, \cos\theta\right), \qquad (1.38)$$

$$l'_{CS} = \frac{q}{2}\left(1, -\sin\theta\cos\phi, -\sin\theta\sin\phi, -\cos\theta\right), \qquad (1.39)$$

Where θ and Φ are the polar and the azimuthal angles, respectively (see figure 1.5b).
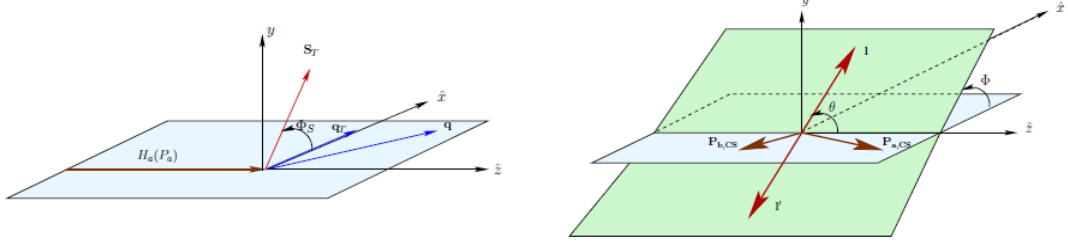
(a) Target rest frame. The definition of the azimuthal angle Φ_S of the proton spin.

(b) The Collins-Soper frame. Definition of polar and azimuthal angles θ and Φ.

Figure 1.5: Definition of the angles of reference frames for DY. Note that P_a and P_b are P_π and P_p, respectively (taken from [5]).

The general formula for the DY cross-section was derived in [11]. If we assume the factorization theorem [4], it was shown that at high energies (s, $q^2 \gg M_\pi^2$, M_p^2) and low transverse momentum ($q_T \ll q$) the cross-section can be expressed as a weighted convolution of TMDs where following shorthand notation is used:

$$C\big[w(k_{\pi T}, k_{pT}) f_1 f_2\big] = \frac{1}{N_c} \sum_i e_i^2 \int \delta^{(2)}(q_T - k_{\pi T} - k_{pT}) w(k_{\pi T}, k_{pT})$$
$$\times \big[f_1^i(x_\pi, k_{\pi T}^2) \bar{f}_2^i(x_p, k_{pT}^2) + \bar{f}_1^i(x_\pi, k_{\pi T}^2) f_2^i(x_p, k_{pT}^2) \big] d^2 k_{\pi T} d^2 k_{pT} \tag{1.40}$$

Where the N_c is a number of colors and $f_i(x, k_T^2)$ are the TMDs. Now, for the case of transversely polarized target and under the terms surviving in the leading-order (LO) QCD parton model [11], we get:

$$\frac{d\sigma}{d^4 q d\Omega} \overset{LO}{=} \frac{\alpha^2}{Fq^2} \hat{\sigma}_U \Big\{ \big(1 + D_{[\sin^2 \theta]} A_U^{\cos 2\phi} \cos 2\phi\big)$$
$$+ |\vec{S}_T| \Big[A_T^{\sin \phi_S} \sin \phi_S + D_{[\sin^2 \theta]} \big(A_T^{\sin(2\phi + \phi_S)} \sin(2\phi + \phi_S), \tag{1.41}$$
$$+ A_T^{\sin(2\phi - \phi_S)} \sin(2\phi - \phi_S) \big) \Big] \Big\}$$

Where the spatial angle Ω denotes the orientation of the muon and:

$$F = 4\sqrt{(P_\pi P_p)^2 - M_\pi^2 M_p^2} \ , \ \hat{\sigma}_U \overset{LO}{=} F_U^1 (1 + \cos^2 \theta), \text{ and } D_{[f(\theta)]} \overset{LO}{=} \frac{f(\theta)}{1 + \cos^2 \theta}. \tag{1.42}$$

Parameter F stands for the flux of incoming pions, $D_{[f(\theta)]}$ is so-called depolarization factor, and $\hat{\sigma}_U$ denotes the part of the cross-section that survives the integration over azimuthal angles Φ and Φ_S. The non-vanishing asymmetries at LO are given as the fractions of the corresponding structure functions to the unpolarized structure function defined:

$$F_U^1 \overset{LO}{=} C\big[f_1 \bar{f}_1 \big]. \tag{1.43}$$

As follows:

$$A_U^{\cos 2\phi} \overset{LO}{=} C\left[\frac{2\left(\vec{h}.\vec{k}_{\pi T}\right)\left(\vec{h}.\vec{k}_{pT}\right)-\vec{k}_{\pi T}.\vec{k}_{pT}}{M_\pi M_p F_U^1} h_1^\perp \bar{h}_1^\perp\right], \qquad (1.44)$$

$$A_U^{\sin\phi_S} \overset{LO}{=} C\left[\frac{\vec{h}.\vec{k}_{pT}}{M_p F_U^1} f_1 \bar{f}_{1T}^\perp\right], \qquad (1.45)$$

$$A_T^{\sin(2\phi+\phi_S)} \overset{LO}{=} -C\left[\frac{2\left(\vec{h}.\vec{k}_{pT}\right)\left[2\left(\vec{h}.\vec{k}_{\pi T}\right)\left(\vec{h}.\vec{k}_{pT}\right)-\vec{k}_{\pi T}.\vec{k}_{pT}\right]-k_{pT}^2\left(\vec{h}.\vec{k}_{\pi T}\right)}{4M_\pi M_p^2 F_U^1} h_1^\perp \bar{h}_{1T}^\perp\right], \quad (1.46)$$

$$A_T^{\sin(2\phi-\phi_S)} \overset{LO}{=} -C\left[\frac{\vec{h}.\vec{k}_{\pi T}}{2M_\pi F_U^1} h_1^\perp \bar{h}_1\right], \qquad (1.47)$$

Where $\vec{h} = \vec{q}_T / q_T$ and subscripts U and T denotes the polarization-independent and transverse-polarization-dependent asymmetries, respectively. Finally we note that measurement of these asymmetries:

➢ $A_U^{\cos 2\Phi}$ gives access to the Boer-Mulders function of the pion beam,

➢ $A_U^{\sin\Phi_S}$ leads to the Sivers function of the target proton,

➢ $A_T^{\sin(2\Phi+\Phi_S)}$ to the Boer-Mulders function of the beam pion and to so-called pretzelosity function $h_{1T}^\perp$ of the target proton,

➢ $A_T^{\sin(2\Phi-\Phi_S)}$ gives access to the Boer-Mulders function of the beam pion and to the transversity function h_1 of the target proton.

If we get beyond the LO, then more asymmetries emerge. But within the QCD TMDs approach they remain kinematic corrections of higher order in q_T/q. For the general cross-section and asymmetries of the higher order of QCD, see [11]. For the specific expectations from the measurement of the asymmetries, see [2].

1.6 J/ψ production mechanism and J/ψ – DY duality

J/ψ is a vector boson consisting of a charm quark c and a charm antiquark $\bar{c}$. The mechanism of its production has been studied in many experiments; however, in spite of wealth of the experimental data, the mechanism still remains unclear [2]. J/ψ with its rest mass $M_{J/\psi} = 3.1$ GeV, can be produced in following reaction:

$$H_a + H_b \rightarrow J/\psi + X \rightarrow l^- + l^+ + X, \qquad (1.48)$$

Where the meaning of its terms was explained earlier (see (1.1)). The cross-section of this reaction consists of the contributions from quark-antiquark and gluon-gluon interactions. And if the angular dependencies are included the lack of data prevents to construct a model for quantitative predictions. The solution of this problem was found in a model based on the close analogy (duality) between the J/ψ production (1.48) and the DY process (1.29). In the $q\bar{q}$ dominance region, as both J/ψ and γ are vector particles and the helicity structure of $q\bar{q}(J/\psi)$ and $(q\bar{q})\gamma^{*}$ couplings is the same, the cross-section of the J/ψ production can be obtained from the DY one by simple replacement [2]:

$$16\pi^2\alpha^2 e_q^2 \rightarrow \left(g_q^{J/\psi}\right)^2\left(g_l^{J/\psi}\right)^2 \, , \, \frac{1}{M^4} \rightarrow \frac{1}{\left(M^2 - M_{J/\psi}^2\right)^2 + M_{J/\psi}^2\Gamma_{J/\psi}^2} \, , \quad (1.49)$$

Where $M^2 \equiv q^2$ is the squared invariant mass of the dilepton pair and $\Gamma_{J/\psi}$ is the width of J/ψ peak. It is believed that this model can be applied for both the polarized and unpolarized cases. In large Bjorken x region (so-called region of u-quark dominance [2]) all couplings cancel in ratios (like the asymmetries), thus they become the same for DY and J/ψ production. If the model is valid, it would enable to use J/ψ production region for extracting the PDFs. This noticeably helps the analysis as the dilepton production counting rate is about 30 times higher in this region than in DY continuum above the J/ψ mass. As the certain region of DY continuum, 4-9 GeV, has much smaller counting rate, the J/ψ data will come to use.

2. Layout of the COMPASS spectrometer

In the following section we will give a brief overview of the COMPASS spectrometer layout, data acquisition system and a special focus will be put on the polarized target. More technical details about the spectrometer can be found e.g. in [13, 2] and for more about polarized target see e.g. [7, 15, 16].

2.1 General outline of the apparatus

The COMPASS experiment was approved in 1997 and began data taking in 2002. It is located in the hall 888 in the CERN Prèvessin site as a descendant of experiments like EMC or SMC. It uses the M2 beam line which provides tertiary muon or secondary hadron beams with momenta 160 – 200 GeV and 120 – 280 GeV, respectively [13]. They are produced by the proton beam extracted from the SPS hitting the T6 beryllium target which is placed about 1 km upstream from the experimental hall. The extraction takes place during a so-called spill, which lasts between 5 and 10 seconds. The spill period together with a longer period without beam for COMPASS[10] (mostly 30 to 40 seconds) is called a supercycle. The M2 beam line consists mostly of bending and focusing magnets which also allow to choose the momentum of the beam and the charge sign of the particles (i.e. by setting current in a magnet the specific particles can be chosen).
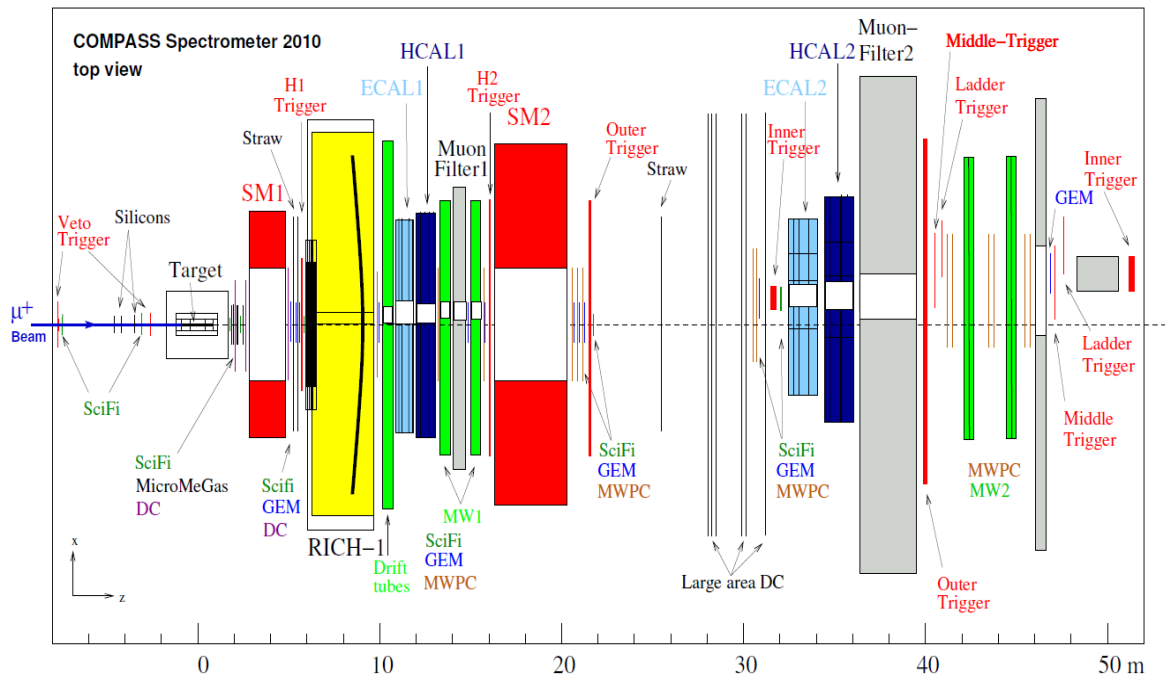

Figure 2.1: The top view of the COMPASS spectrometer [2].

---

[10] The SPS beam is distributed between several experiments.

The COMPASS spectrometer consists of three parts – the detectors upstream of the target, which are responsible for monitoring the beam, then the Large Angle Spectrometer (LAS), and Small Angle Spectrometer (SAS) downstream of the target. A top view on the layout of the whole spectrometer is depicted on the figure 2.1. For a spatial view see figure 2.2.
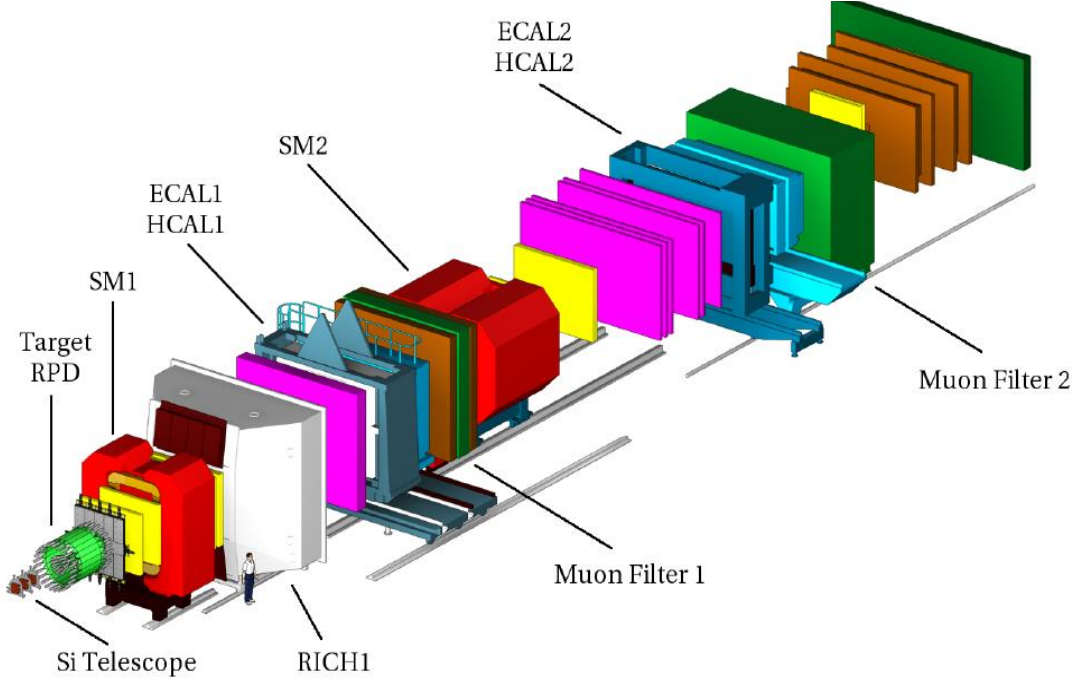

Figure 2.2: Three-dimensional view of COMPASS setup for the hadron beam measurement [14][11].

The LAS surrounds the SM1 dipole magnet (see figures 2.1 or 2.2) which has ±180 mrad acceptance[12] and magnetic field 1.0 Tm. The SAS begins with the SM2 dipole magnet with magnetic field 4.4 Tm (ibid.). Both of them are followed by particle identification detectors, electromagnetic and hadronic calorimeters and plenty of tracking detectors which we will shortly discuss in the following. First to be referred is the tracking system. It is essential for tracking and identifying the charged particles. There are several different types of detectors with decreasing resolution in the direction from the target. First detector is the **Beam telescope** which precisely measures the position of the beam particles. It consists of the Scintillating Fibers (**SciFi**) and **silicon detectors**. The SciFi detectors are

---

[11] In the contemporary setup we use the SciFi instead of the Si Telescope and the polarized target instead of RPD.

[12] The acceptance is defined as the distribution of the reconstructible tracks [13].

used for the track reconstruction rather than the spatial resolution due to their excellent time resolution. Both previously mentioned detectors are called very small area trackers. They are followed by so-called small area trackers. Due to their high spatial resolution they can track the particles close to the beam. There belong the so-called Micromesh gaseous detectors (**Micromegas**) and Gaseous electron multiplier (**GEM**) detectors. Both of the detectors are illustrated on the figure 2.3.
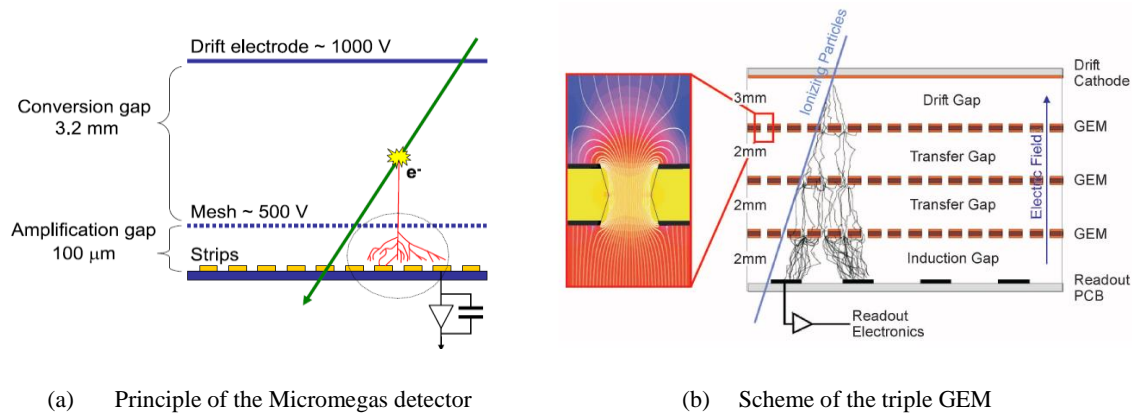
(a)   Principle of the Micromegas detector   (b)   Scheme of the triple GEM

Figure 2.3: Schematic image of the Micromegas and GEM detectors [13]

Then there is the large area tracking system consisting of **Drift Chambers** (DC), **Straw tube detectors** and **Multiwire Proportional Chambers** (MWPC). They have to provide a good spatial resolution on a large area and that is what the chosen gaseous detectors fit the best. Their location can be seen from the figure 2.1.

The detection of the muons is performed by the **muon walls** (MW1 in LAS and MW2 in SAS). They consist of an absorber which filters the muons from the other particles (the MW1 has a 60 cm thick iron wall and the MW2 has 2.4 m thick concrete wall) and several tracking planes. The principle is following: the planes are placed in front of the absorber and behind it as well and when a track detected in the former detector continues to the latter then the particle must be a muon.

Another important group of the detectors are the calorimeters. There are currently two electromagnetic (ECAL1 and ECAL2) and two hadronic (HCAL1 and HCAL2) calorimeters in COMPASS, each type in LAS and SAS. The ECALs are mostly homogeneous calorimeters, which means that the calorimeter modules are made of a lead glass that serves as both the absorber and the scintillator. The modules are read out by photomultipliers. There are about 3000 modules in the central part of the ECAL1. On the other hand, the ECAL2 is a shashlik type calorimeter which denotes altering layers of the absorber and the

scintillator. Both of the calorimeters have a hole in the center to allow passing the non-interacting particles of the beam and the particles scattered at small angles in the case of the ECAL1. The HCALs are both shashlik type. There are 480 modules in HCAL1 and 218 modules in HCAL2. All the signals are read by the multipliers and small part of them is used for triggering.

The important part of the apparatus is the Ring Imaging Cherenkov detector (**RICH**). Its purpose is the identification of the charged hadrons with momenta ranging from 1 GeV to 43 GeV. It is based on the Cherenkov effect i.e. the emission of an electromagnetic radiation when the charged particle is passing through a dielectric medium with velocity higher than the phase velocity of light in that medium [5]. It contains about 80 m^3 of some suitable gas (e.g. C_4F_{10} or N_2). It has to be perfectly transparent thus the gas is usually additionally purified. The reflective part consists of two mosaic mirrors made of 116 hexagonal and pentagonal mirrors. The photo-detection is based on photomultipliers and MWPC detectors equipped by CsI photocathodes which detect the Cherenkov light and convert it to photoelectrons and those are amplified by the MWPC. Another particle identification detector using the Cherenkov effect is the Cherenkov Differential counter with Achromatic Ring focus (**CEDAR**). This detector is placed upstream from the target and provides the identification of the beam particles.

2.2 The Data Acquisition system

The measuring of the data is the initial part of the whole process. The second step is to collect the data from the detectors, to appropriately filter them and perform the first preliminary analysis which composes the data from various detectors to a meaningful set. This is the purpose of the Data Acquisition (DAQ). The overall scheme of the DAQ is depicted on the figure 2.4. The first selection of data is realized by the triggers which give the signal about what data to pass further to the DAQ. The role of the triggers is provided by hodoscopes i.e. detector planes made of scintillators (used for their fast response).

As in the high energy physics the attention is often focused on rare processes, which implies the need for high particle fluxes and the triggers have to filter the interesting events from a tremendous amount of data and be very quick in addition. And even after that massive filtration a large amount of data is left and has to be further processed and stored.

The readout of the detectors is performed by the frontend electronics. The COMPASS detectors have about 300 000 read out channels in total. The average size of a single event is

35 kB and trigger rate is 50 kHz. For the coming DY data taking the expected rate is rather lower, about 30-35 kHz, and the event size 25 kB [2]. The frontend electronics converts the analogue signals to a digital form and sends them through 1000 links into so-called CATCH, HGeSiCa, and Gandalf modules (250 modules in total). These modules are close to the detectors and their main two purposes are to operate the frontend electronics, and to create basic data blocks universal for the rest of the DAQ system. The output of those modules goes to FPGA modules, in some cases through Slink multiplexers or TIGER modules (see figure 2.4). In the Slinks and TIGERs the number of links is reduced to about 90, depending on the number of detectors (currently, there are 75 links [18]). The FPGA takes at most 15 links and reduces them into 1 output link. These modules are connected to the triggers and timing systems which label them with timestamps and event identification. The output data from FPGA are called subevents and denote parts of a particular event [17, 18].
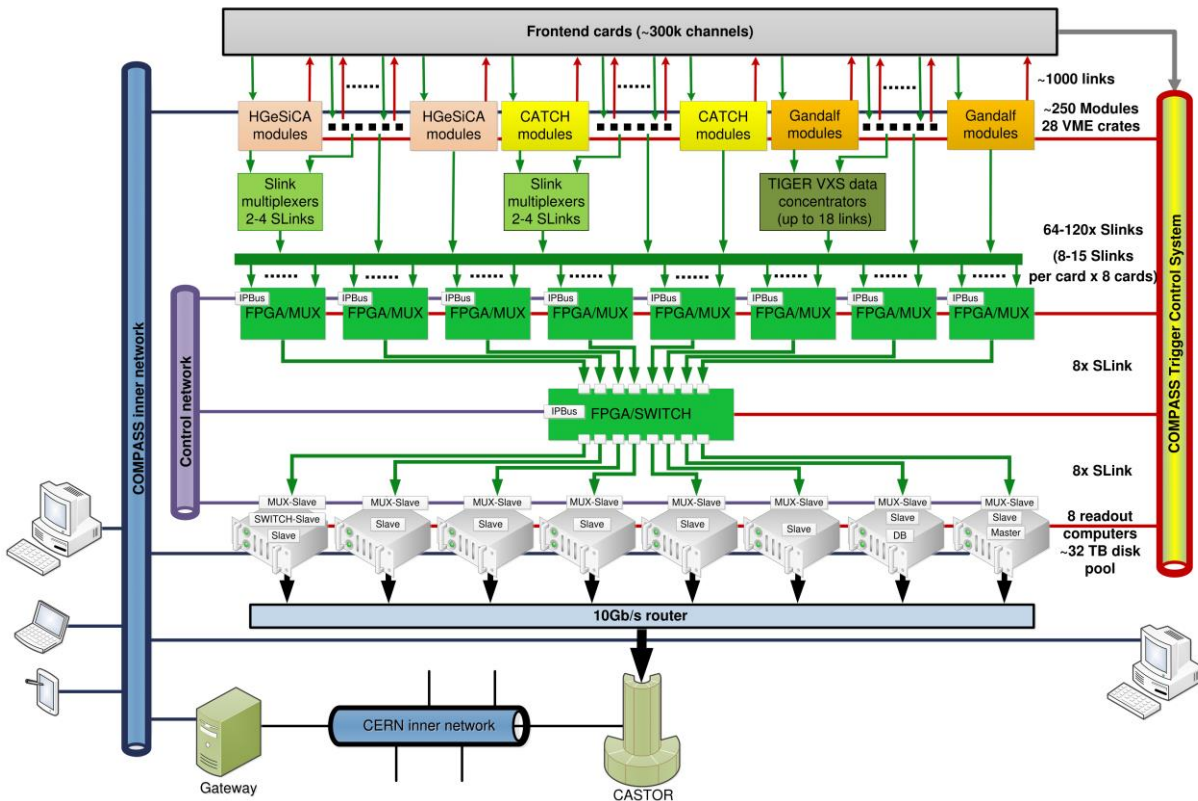

Figure 2.4: The new DAQ hardware [18].

Then the data continue from the FPGA to the SWITCH which combines the corresponding subevents to events and sends them forward to readout PCCORE computers via custom-made spillbuffer cards which further process them and convert them to *date* format. Then the data are temporarily stored to HDDs (about 32 TB at disposal) and about

1% is directly used for the online monitoring. Finally, the data are stored permanently in CERN Advanced STORage manager (CASTOR), the central data storage. From that point, the physicists can approach them and process them further and analyse. For more information about the DAQ or particular modules of the hardware, see [17, 18, or 19].

2.3 The Polarized Target

The polarized target (PT) is the crucial component of the COMPASS experiment for the nucleon spin studies. It enables us to access the TMDs in the case of transverse polarization or in the longitudinal case we can study for example the g_1 structure function or the gluon polarization. The COMPASS polarized target was constructed to gain as high as possible polarization; the main components are strong magnets, cooling device, and a microwave system, which will be briefly discussed in the following. The figure 2.5 shows the schematic picture of the PT layout (the detailed scheme of the PT can be found in Attachment 1).
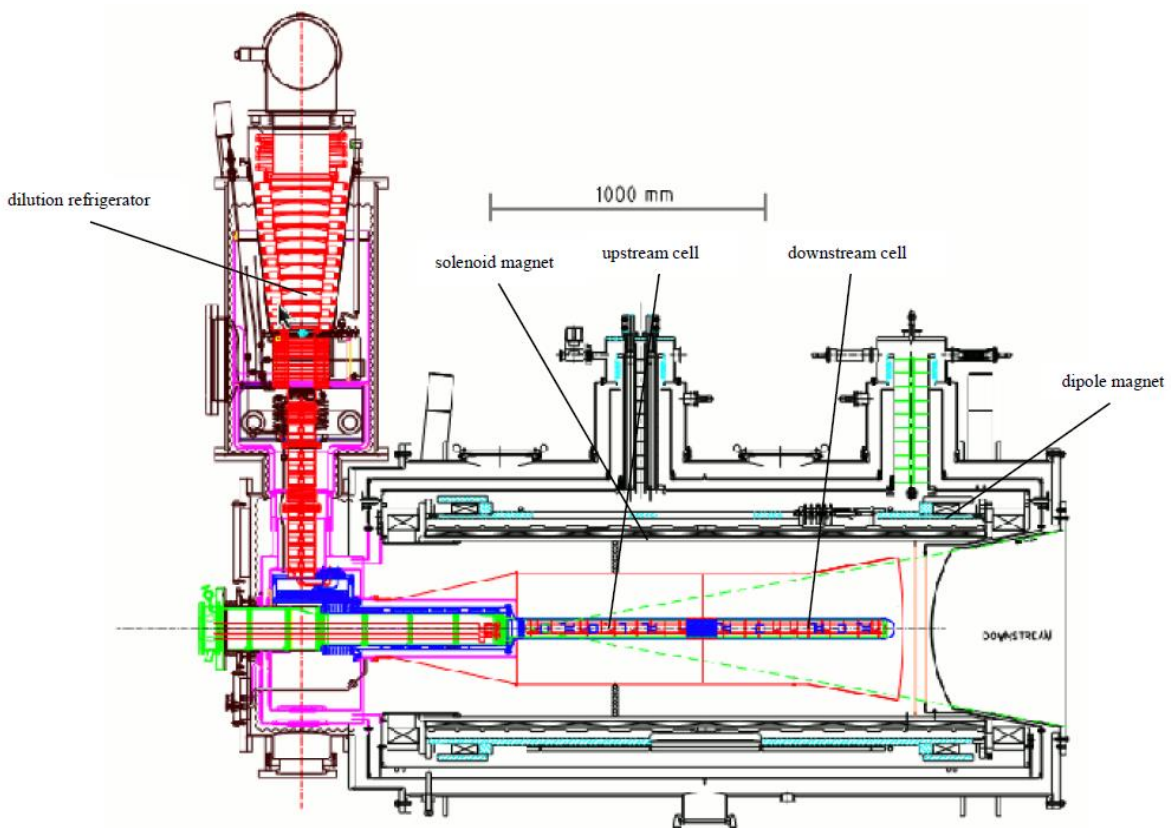

Figure 2.5: The side view of the Polarized target system.

To polarize the target material, its nuclear paramagnetism has to be used. Unfortunately, the nuclear paramagnetism is very weak and the polarization of nuclear spins does not reach a significant level even if in very low temperatures and high magnetic field. Thus, the

Dynamic Nuclear Polarization (DNP) is used, which is a technique of transferring a high electron polarization to the polarization of the nuclei through a radiofrequency field. More about the principles of this method can be found e.g. in [7, 15]. DNP requires temperatures in order of ~100 mK and strong, homogeneous magnetic field. The microwaves are used to transfer the polarization to the nuclei. By this effective method a polarization about 90% can be achieved. The whole target is placed in a dilution refrigerator (DR) which allows to cool the target material down to a temperature of about 70 mK [7]. The magnetic field for the polarization procedure is provided by a 2.5 T superconducting solenoid magnet (see figure 2.5). After the polarization the additional 0.6 T superconducting dipole magnet can be used to rotate the spins of the target material nucleons into a transverse direction[13]. At the mentioned temperature the relaxation times of nuclear spins are very long[14], which enables the measurement with the transverse polarization. A photograph of the whole device can be seen in Attachment 2.
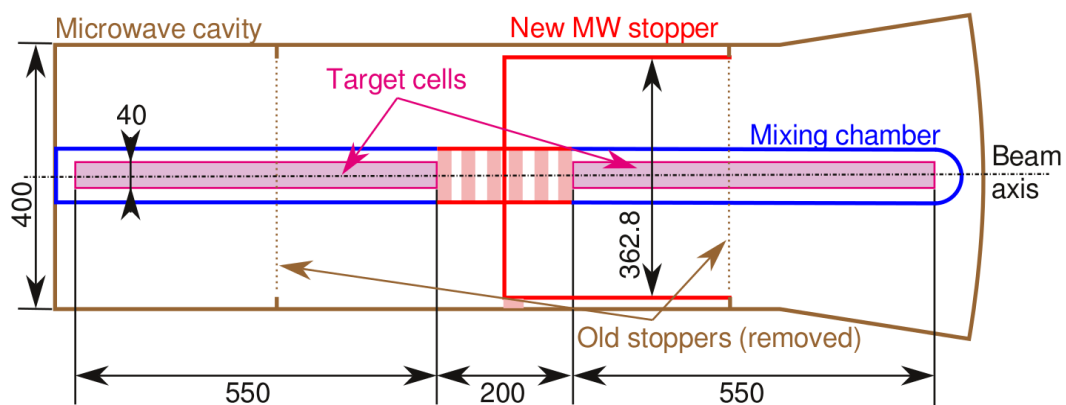

Figure 2.6: The Polarized target and the microwave cavity in more detail.

Now we will shortly describe the principle of DR. There is a mixture of liquid ^{3}He and ^{4}He with specific concentration of ^{3}He. The mixture is cooled down to the temperature of about 1 K. Then it undergoes a phase separation of both components, i.e. the mixture splits up: a phase rich on the ^{3}He (concentrated phase) starts to float on the phase rich on the ^{4}He (diluted phase). There is a capillary inside the DR that connects vessels containing the concentrated and the diluted phases. The pressure above the surface of the diluted phase is lowered using powerful pumps. The ^{3}He evaporates much more easily, so the diluted phase

---

[13] This process of the field rotation occurs as the solenoid is ramped down after the creation of the polarization, and the dipole is ramped up.

[14] They reach about 4000 hours for the ammonia in the transverse field [5].

gets ^{3}He-depleted. Consequently, the atoms of ^{3}He are forced to cross the boundary between the two phases. This is where the actual cooling takes place. It is analogous to the classical evaporation, the role of the vacuum being played by the ^{4}He atoms. The ^{3}He vapors are compressed, purified, cooled in heat exchangers and returned back to the concentrated phase, allowing a continual operation. The space where both of the separated phases are kept is called the dilution (or mixing) chamber (in the COMPASS PT it directly surrounds the target cells; see the figure 2.6). The DR is equipped by 36 thermometers for monitoring the temperatures and several pressure gauges, valve controls, and flow meters for checking the ^{3}He and ^{4}He flows. This entire monitoring device is connected directly to a computer where other monitoring software runs. Additional technical details of the DR can be found for example in [7].

The PT itself consists of 2 cells with opposite polarization, the upstream and the downstream one, each of 4 cm in diameter (see figure 2.6) and 55 cm long[15]. The reason for having two separate cells instead of one is that the asymmetries cannot be extracted from consecutive measurements on the same target with switched polarizations because of the variations of relative beam flux. The systematic error of the measurement would be too high. Each cell contains 5 NMR (Nuclear Magnetic Resonance) coils which provide a precise measurement of the nuclear polarization (for more about NMR polarization measurement in COMPASS see e.g. [5, 7]). The target cells are both placed in the dilution chamber, which is inside the microwave cavity that is placed in the superconducting magnet which we mentioned above (see figure 2.6).

The purpose of the microwave system is to irradiate the target material by microwaves at frequency of about 70 kHz. The microwave cavity is the key component of this system. The cavity creates the standing microwaves of given frequency inside its volume which is divided to two parts by a microwave stopper, as can be seen on the figure 2.6. This setup allows the operation at different frequencies in upstream and downstream cell which is necessary to gain the opposite polarizations. The cavity is cooled by liquid helium to a temperature of about 4 K. The most of the rest of the system consists of two microwave generators.

The choice of the target material is a very important point for the right function of the polarized target. It is necessary for precise measurement of the asymmetries i.e. for the

---

[15] It is a new setting used for the DY run, for the old configuration of PT see e.g. [7, 13].

highest possible statistics. The properties of the material can be expressed by the formula called Figure of merit F_{oM}:

$$F_{oM} = f^2 P^2 \rho F_p ,$$

(2.1)

Where F_p is a packing factor; ρ is the target material density; P is a maximum possible polarization of the material; and f is the dilution factor which denotes the fraction of events on polarized nuclei with respect to the unpolarized ones. It can be defined as follows:

$$f' = \left(1 + \frac{n_A \sigma_A}{n_p \sigma_p} \right)^{-1} ,$$

(2.2)

Where σ_A is a cross-section for an unpolarized nucleus, σ_p is a cross-section for a polarized one, and n_A and n_p are molar densities for the particular nuclei.

In the past COMPASS and SMC experiments there was need for a neutron target, thus the deuterated materials as ^{6}LiD or deuterated butanol were used. For the contemporary DY experiment the ammonia is going to be used. Liquid ammonia is frozen down by liquid nitrogen and forms small beads with 4 mm in diameter. The NH_2 radicals needed for the DNP are produced by irradiating the material with 20 MeV electron beam at low temperature at the Bonn University linac. The maximum polarization that is achievable is over 95% while the usual polarization achieved at COMPASS was between 80 and 90 % [7]. The dilution factor of the ammonia is 0.15 in average.

3. Feasibility of Drell-Yan measurements at COMPASS

In the following section we first describe the experimental setup for the DY measurement at COMPASS. Then we discuss shortly the Monte Carlo simulations of the COMPASS experimental conditions and its results. In the third and the fourth subsections, we introduce the conditions of the 2009 DY test beam and the 2014 DY data-taking, respectively. Then, the analysis of the dimuon pair production and the several kinematic distributions are given. As the target from these data-taking periods was not polarized, we can't have an access to any of the spin asymmetries, hence only the basic properties of the dimuon production can be studied. Finally, in the last subchapter we give a brief outline of the expectations for the ongoing 2015 data taking.

3.1 The setup of the DY program at COMPASS

In order to access spin structure information by the Drell-Yan process a high-intensity hadron beam and a large-acceptance set up as well as a high-performance polarized target are needed. Such equipment is provided by the COMPASS spectrometer. COMPASS will be using 190 GeV π^- beam of intensities up to 10^9/spill, detection system capable to stand high particle flux, and the transversely polarized target with high polarization. The beam is produced by the SPS 400 GeV proton beam hitting a beryllium target, as was described above. It contains approximately 97% of pions, 2.3% of kaons and the rest are antiprotons and other particles [13].
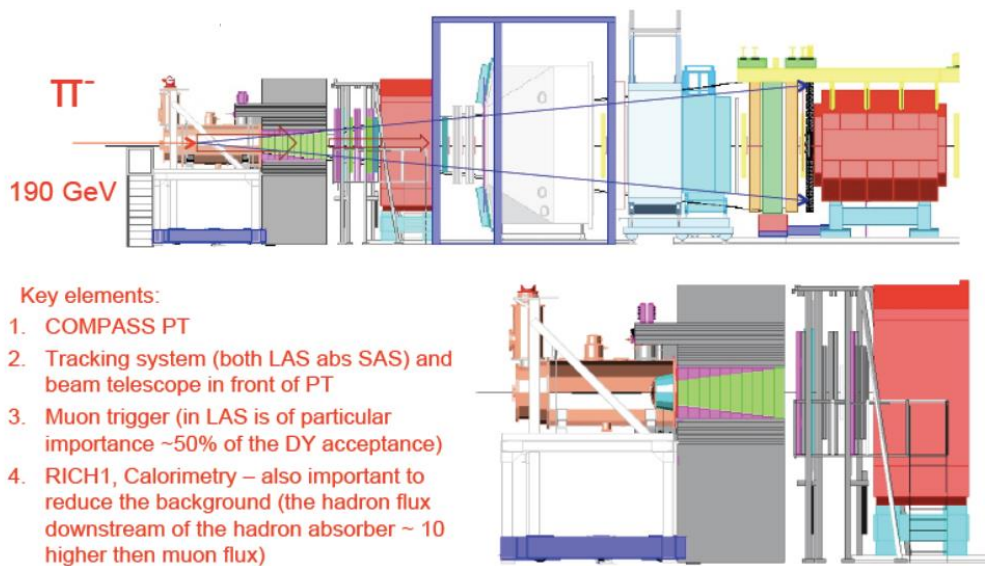

Figure 3.1: The scheme of the COMPASS spectrometer for DY measurement [20].

Based on the 2007 and 2008 DY beam tests [2] there have been some upgrades of the experimental setup. The most important is the installation of the **hadron absorber**. The purpose of the absorber is to reduce the high secondary hadron and electron flux produced by the interaction of the beam in the target and to lower the occupancies of trackers. This will make the muon detection easier because they have a very long mean free path and most of them would be just slightly elastically scattered in the absorber.

The choice of the absorber material had to follow two main criteria: to maximize the number of interaction lengths crossed by the produced hadrons in order to stop them while minimizing the radiation lengths in order to have a minimal energy loss and to minimize multiple scattering of muons. The model of the absorber was tested in 2009 test beam and the results were satisfactory [2]. The position of the hadron absorber is shown on the figure 3.1. The absorber consists of the tungsten beam plug which is supposed to stop the beam[16] which is inside the main part made of alumina (Al_2O_3) and contained in stainless steel block. It is all covered with additional concrete shielding to protect the target electronics and reduce the radiation dose spread in the hall.

The negative effect of the absorber lies in the increased multiple scattering of DY dimuons (i.e. muon pair) which makes the vertex reconstruction less precise. Thus, there would be an increased migration from one target cell to another, which would result in smaller asymmetries at the end [5]. One of the solutions used to minimize this statistical error was to enlarge the gap between the target cells to 20 cm. Another solution was the installation of the so-called **vertex detector** between the target and the absorber (in principle, it is a SciFi detector). This detector should help to improve the resolution of the vertex reconstruction by a factor of 5 [2].

The planned beam intensity for the DY program is 5×10^8 hadrons per spill (about 10 seconds) which together with the hadron absorber will lead to increase of the radiation dose in the hall. This expectation was confirmed by the 2009 test beam (with maximum beam intensity 1.5×10^8/spill). This led to reinforcement of the concrete shielding around the absorber and to repositioning of the access door to the experimental zone to reduce the radiation dose. For the same reason, the control room has been moved to a remote control room which is located in an office building (no. 892).

---

[16] In the previous experiments the configuration with no beam plug but just a hole filled with air was tested in order to prevent backscattering of the beam particles into the target, but it wasn't successful.

3.2 Monte Carlo simulations for the DY program

The interpretation of the physics processes of interacting hadron beams and several particles in a final state requires a deep understanding of the experimental setup. This can only be achieved by a realistic simulation of all the experimental conditions, the whole apparatus with detailed knowledge of the acceptance as a function of any particular kinematic variable. The Monte Carlo (MC) method serves well this purpose. For simulating the beam, the track parameters used to generate the beam and the beam halo are taken from the real data recorded with randomly generated triggers. The parameters of the beam particles are extracted from the tracks reconstructed by the SciFi trackers. The parameters of the near halo are taken from halo tracks reconstructed along the spectrometer. And the far halo component which is falling outside the spectrometer acceptance, the momentum is assigned using the parametrization from the MC simulation of the beam line. For generating the leptons, photons, or hadron interactions, e.g. the MC generators Lepto, Aroma, and Pythia codes are used [13]. The propagation of the final state particles through the COMPASS setup is performed by the MC code called COMGEANT [11]. The multiple scattering, energy loss, electromagnetic showers, and secondary interactions are taken into account so as hadron in-flight decays or interactions.

The interactions are generated randomly inside the target and secondary tracks are propagated through the spectrometer. The material and type of elements of the spectrometer is described by a material map which carries the information about the type of the material and its amount. It consists of three dimensional grids with variable cell size, which depends on the homogeneity of the particular material. The relevant information like density or radiation length about every cell is stored. Material maps are defined around the target, between the target and the SM1, between the SM1 and RICH, the RICH itself and the muon filters [13]. The materials of all those components are taken into account for computing the spectrometer acceptance including the detector frames, support structures, and hadron absorbers. For simulating the detector response, there are two main quantities considered, the efficiency and resolution. Only in case of some specific detectors, as RICH, calorimeters or GEM, the space and amplitude distributions are also simulated. All the detectors simulations have been tuned according the real measurements.

When the events are simulated, they are processed by the COmpass Reconstruction and AnaLysis (CORAL) software which is used for the track reconstruction (the same procedure

takes place in case of the real data; for more about event reconstruction see [11]). The tracks of charged particles are reconstructed from the simulated hits in the tracking detectors using the same procedure as for the real data. The CORAL outputs mDST ("mini Data Summary Trees") which can be proceeded directly to the analysis software PHAST (PHysics Analysis Software Tool) where the final analysis takes place and the simulated data can be compared with the real ones. The MC simulations serve as a crosscheck with the ongoing measurement or a prediction of expected processes when it precedes the data taking.

3.3 The analysis of the 2009 pilot run[17]

3.3.1 Data taking conditions

A three days lasting DY beam test using the hadron absorber was performed in COMPASS at the end of the data-taking period of 2009, between 19th and 23th November [21]. There were 51 successful runs taken. As it was already mentioned, a π^- beam with momentum 190 GeV was used. The average intensity was 8×10^7 π^-/spill (spill length of 9.6 s), except of two runs where the intensity reached 1.5×10^8 π^-/spill. The beam spot was focused with $\sigma_{x,y} \approx 0.3$ cm in the target. The current in the SM2 dipole magnet was set to 5000 A. The target was made of two cells of polyethylene (CH_2) and had 40 cm in length and 5 cm in diameter, the distance between the cells was 20 cm. The upstream target cell was positioned at $z =$ [-233, -193] and the downstream one at $z =$ [-173, -133] (the z coordinate is taken from the standard COMPASS coordinate system [21]). The hadron absorber was positioned downstream of the target, at $z =$ [-113, 87]. It was made of one block of concrete and one block of non-magnetic stainless steel, and in the central part of the absorber there was a beam plug made of 6 cylinders of tungsten followed by 2 of stainless steel ones with increasing diameter with respect to the beam direction [22].

Some trigger modifications took place in order to provide a dimuon trigger, the first one using the hodoscopes in the SAS (Middle, Ladder and Outer hodoscopes) in coincidence with a signal from the HCAL1 trigger in the LAS (so called double_1); and the second based on two signals in HCAL1 (double_2). In addition, there were some single muon triggers.

---

[17] In the following sections 3.3 and 3.4, in all the histograms or graphs depicting mass or momentum distribution the convention $c = 1$ is not used. However, in the text it still applies.

3.3.2 The results of the 2009 test beam

The first production of the data was performed in 2010 (see [21]). However, a second production had to be made in 2012 because of several problems with the standard vertexing procedure in CORAL[18]. Hence, some additional adjustments of CORAL procedure were performed (for the complete list, see [22]). From the created mDSTs, the µDSTs (micro Data Summary Trees) were produced selecting the events with at least one primary vertex and exactly two outgoing charged particles. Then, some additional selections had to be applied for choosing the right event candidates. They are described as follows [22]:

1. Events with the primary vertex within a target position of z = [-263, -103] cm together with the margin $\pm$ 30 cm with respect to the target limits to avoid events coming from the absorber. If there is more than one primary vertex, than the best primary vertex (the PHAST function iBestPrimaryVertex) is preferred. Otherwise, the primary vertex with the smallest vertex χ^2 is chosen.

2. Then, only the events with $\mu^+\mu^-$ pair are chosen. It is executed by a PHAST function PID() which assigns a muon identification to every particle crossing more than 30 x/X_0 along the spectrometer (more about mean free path condition in the spectrometer, see [22]).

3. Choosing the double trigger only.

4. The trigger validation to ensure that the selected muons are the ones that fired the trigger. In case of double_1 system, one muon has to have one associated cluster in the calorimeter or at least 4 hits in the second part of MW1 and the other muon has to point to the SAS hodoscope pair having fired the muon, or it has to have some hits in the outer trigger system if it came from the outer system. And in the case of double_2, each of the muons has to have an associated cluster in calorimeter or at least 4 hits in the second part of MW1.

5. Events with p_μ < 100 GeV to reject the muons which were created in the pion beam decay (for more details about the decay, see [22]). The figure 3.3 shows the kinematic distributions of both muons before this selection cut (a), and right after the cut (b).

---

[18] The standard vertexing procedure performed by CORAL was not suitable for the used experimental settings because of the large amount of material on the target region (namely caused by the hadron absorber) [21].

6. The cut on the more narrow target position of the primary vertex, $z =$ [-253, -113] cm. On the figure 3.4 the impact of this cut is depicted.

7. $r_{vtx} < 1$ cm (~ 3σ of the beam spread). This selection is shown on the figure 3.5.

8. $Z_{last} < 1750$ cm which rejects all the events with tracks not passing through MuonFilter1.

9. $Z_{first} < 300$ cm which cuts all the tracks starting before the SM1.

The statistics and the results of the all the processed data analysis can be found in [22]. In the following, we provide our own analysis of a selected part of the newest, the 3rd production of data (19 runs with 1904 spill in total) using the same selection criteria, except the trigger validation. The list of the selections together with their impact on the statistics is presented in table 3.1. The dimuon mass distribution with a visible cleaning effect on the statistics follows in figure 3.2.

	Cut	# events		statistic [%]							
	microDST	35731693	100								
1.	Prim. vtx from the target region	6755666	18.9	100							
2.	$\mu^+ \mu^-$ pair	2428274	6.8	35.9	100						
3.	Double trigger	1170883	3.3	17.3	48.2	100					
4.	$p_\mu < 100$ GeV	777203	2.2	11.5	32.0	66.4	100				
5.	-253 < Z_{vtx} < -113 cm	683782	1.9	10.1	28.2	58.4	88.0	100			
6.	$r_{vtx} < 1$ cm	670887	1.9	9.9	27.6	57.3	86.3	98.1	100		
7.	$Z_{last} > 1750$ cm	282739	0.8	4.2	11.6	24.1	36.4	41.3	42.1	100	
8.	$Z_{first} < 300$ cm	240922	0.7	3.5	9.9	20.6	31.0	35.2	35.9	85.2	

Table 3.1: The impact of each selection on the statistics.

The comparison between the official statistical results and our own outcome is not presented because we have used a bit different order of the selection criteria in our calculations, thus it doesn't completely correspond to the official results.
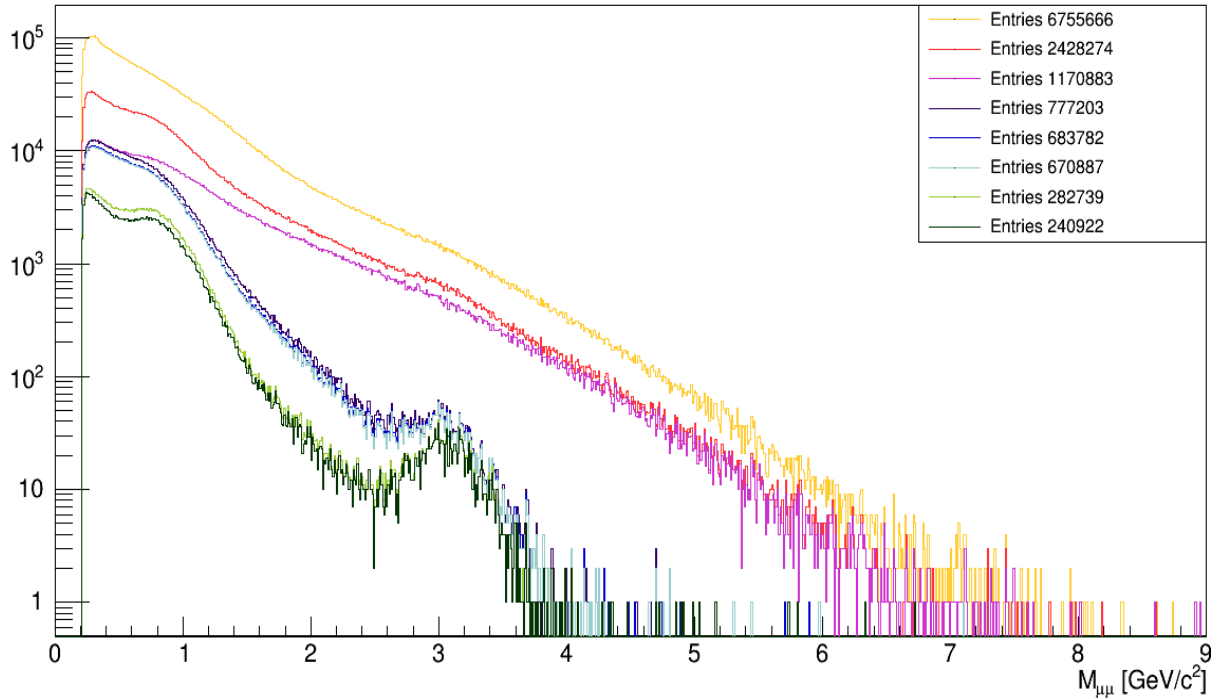
Figure 3.2: The impact of each selection criterion in dimuon mass distribution.
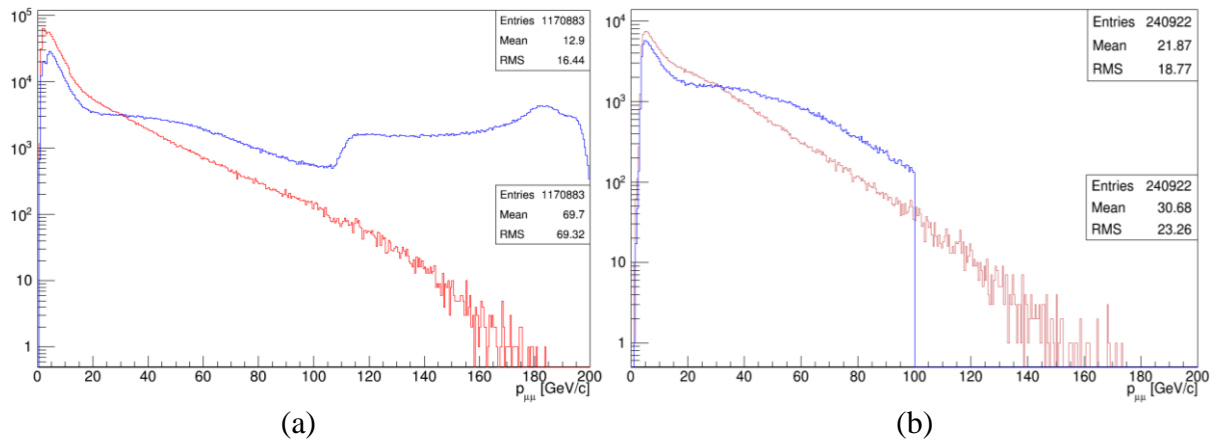

Figure 3.3: The kinematic distribution for μ^+ (red) and μ^- (blue) before (a) and after (b) the cut of μ^- coming from the pion decay.

The figure 3.4 shows the comparison (a) between the distribution of all the muon mass (blue distribution), and of muon mass larger than 2.5 GeV (red). It can be seen that in the former case, the two cells cannot be distinguished one from another while in the latter the cells are clearly visible. In the red distribution, the Z_{vtx} cut is also visible.

(a)

(b)
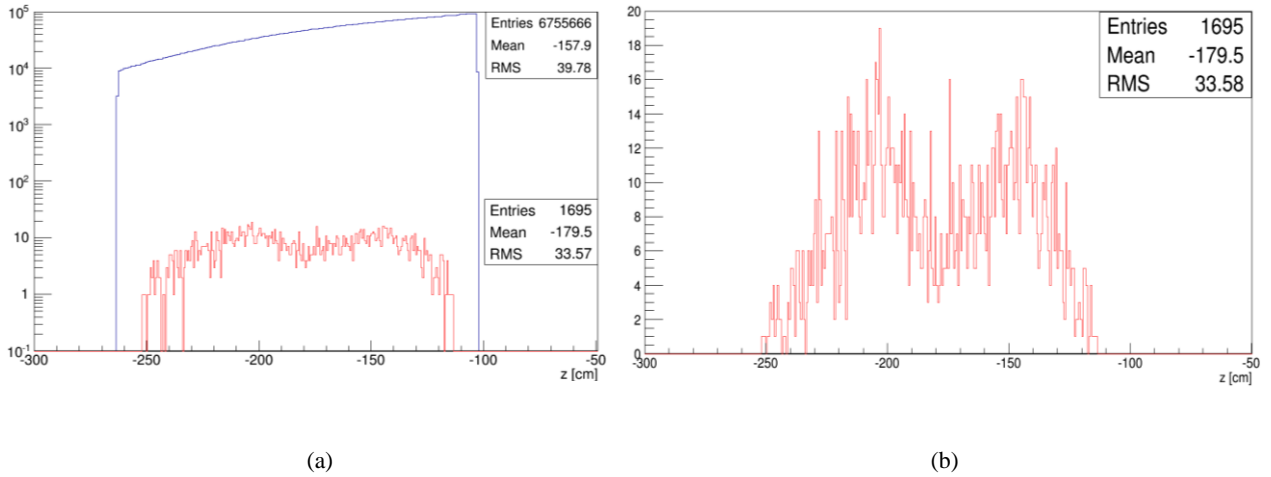
Figure 3.4: Z vertex distribution. It shows the comparison (a): if the higher muon mass is not selected (blue distribution), and in case of muon mass larger than 2.5 GeV (red distribution), in logarithmic scale. In (b) only the higher muon mass in linear scale is shown.

(a)

(b)
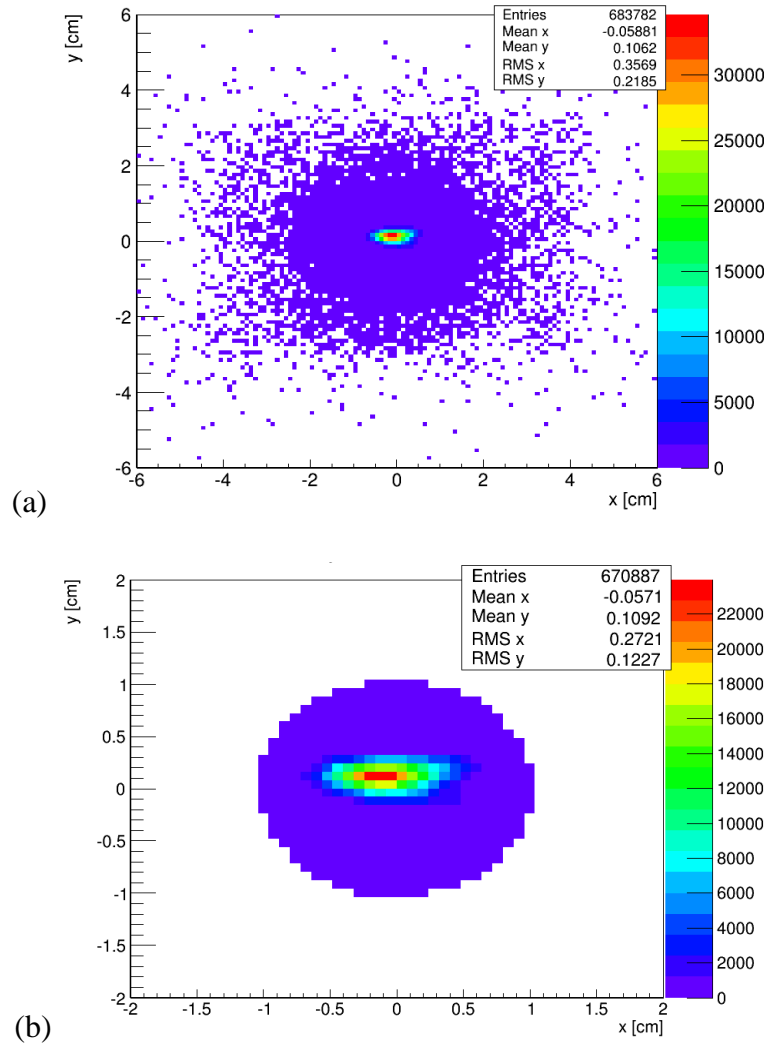
Figure 3.5: X_{vtx} versus Y_{vtx} distribution of the beam (a). The cells have 2.5 cm radius and the beam spreads out in $\sigma = 3$ mm. The cut is presented on the figure (b).

The figure 3.6 shows the dimuon mass distribution produced using the selection cuts. The number of high muon mass in the DY continuum ($M_{\mu\mu} > 4$ GeV) is very low due to the short duration of the beam test and also only 19 runs from 51 existing being processed. On the other hand, the statistics is considerably better in the 3rd data production than in the 2nd (for the details, see [23]), but as can be seen from the figure 3.6, the number of high mass muons is still negligible. Thus, the J/ψ production is used to make some conclusions.
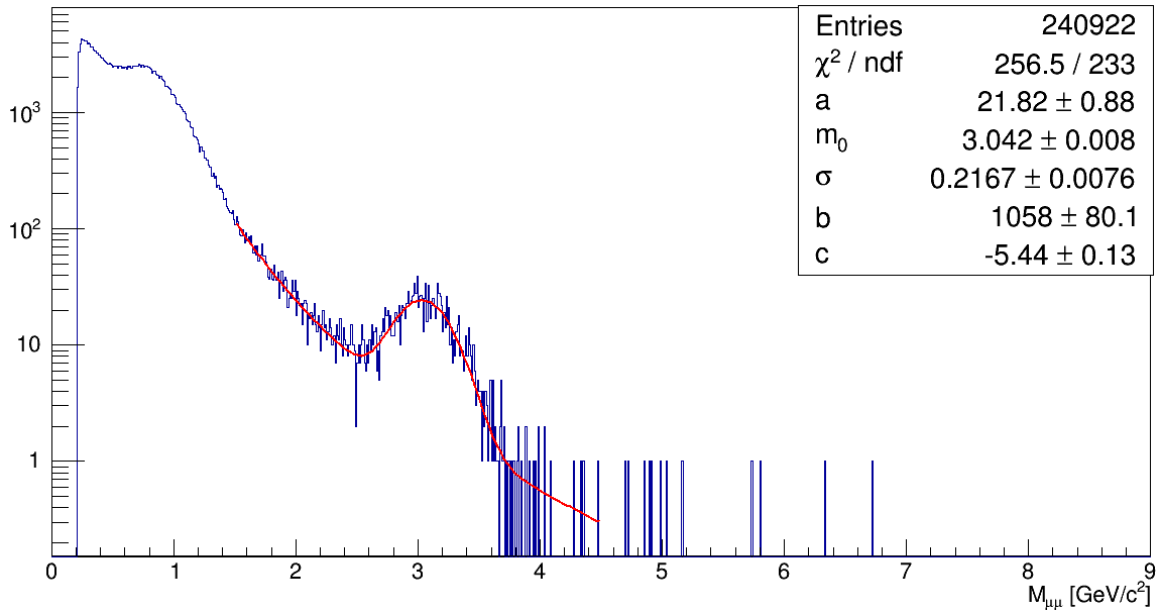
Figure 3.6: Dimuon mass distribution of data after all cuts with fitted J/ψ peak. a denotes the amplitude, m_0 is the mass of J/ψ, σ is the resolution of the J/ψ mass region.
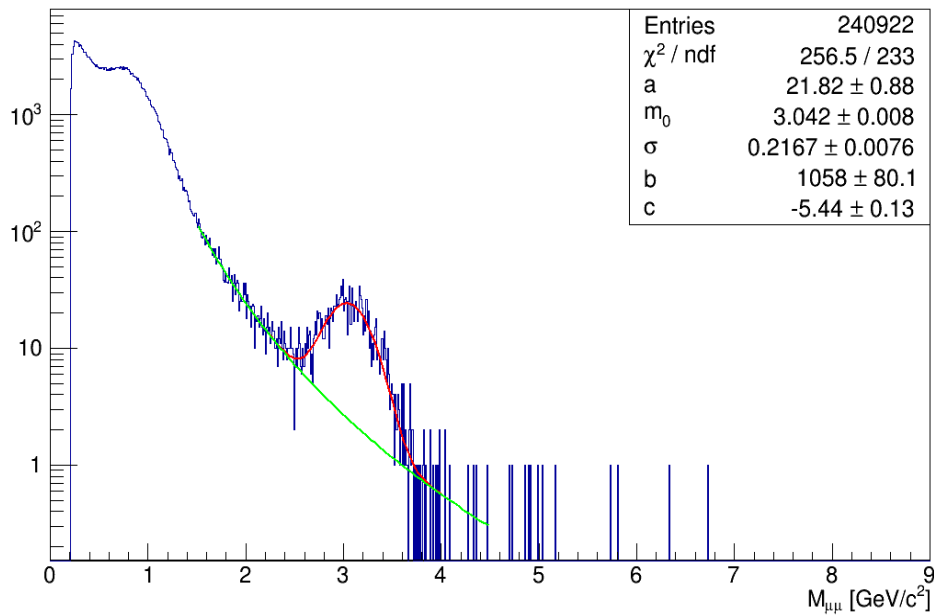
Figure 3.7: The background processes of J/ψ production (in green).
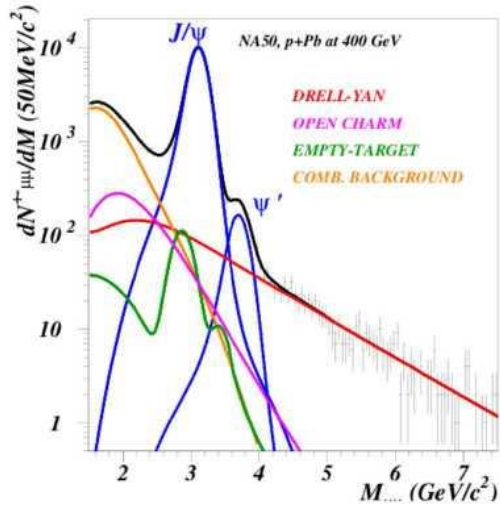
Figure 3.8: Major background processes of dimuon mass distribution [5].

We used a Gaussian function plus a power law function $b \cdot M^c_{\mu\mu}$ (from [22]; the parameters are used from the figure 3.6) in the range 1.5 to 4.5 GeV as a fitting function. As can be seen from the figure 3.8, there is another background process that peaks in the region, the production of ψ' (excited state of J/ψ), but that is neglected here. Integrating the fitting function in the range of 2σ and subtracting the background (as seen in figure 3.7), one gets 1130 ± 120 J/ψ events with a mean mass of 3.042 ± 0.008 GeV and mass resolution of 217.6 ± 7.6 MeV. These results are in agreement with the 3rd data production analysis [23].

Concerning triggers, it was already explained above that two dedicated double triggers were used. The figure 3.9 shows the distribution for the complete trigger mask[19] (a) and the distribution for given triggers after the application of the trigger mask for the double_1 and double_2.

(a)

---
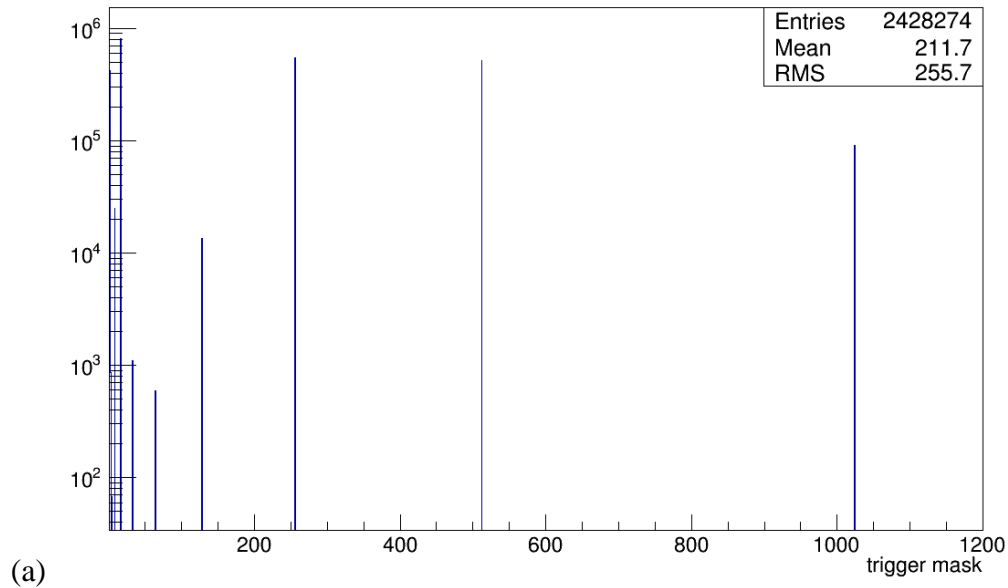
[19] The trigger mask is a 12-bit number, with each bit denoting whether the corresponding trigger condition was satisfied of not.

(b)
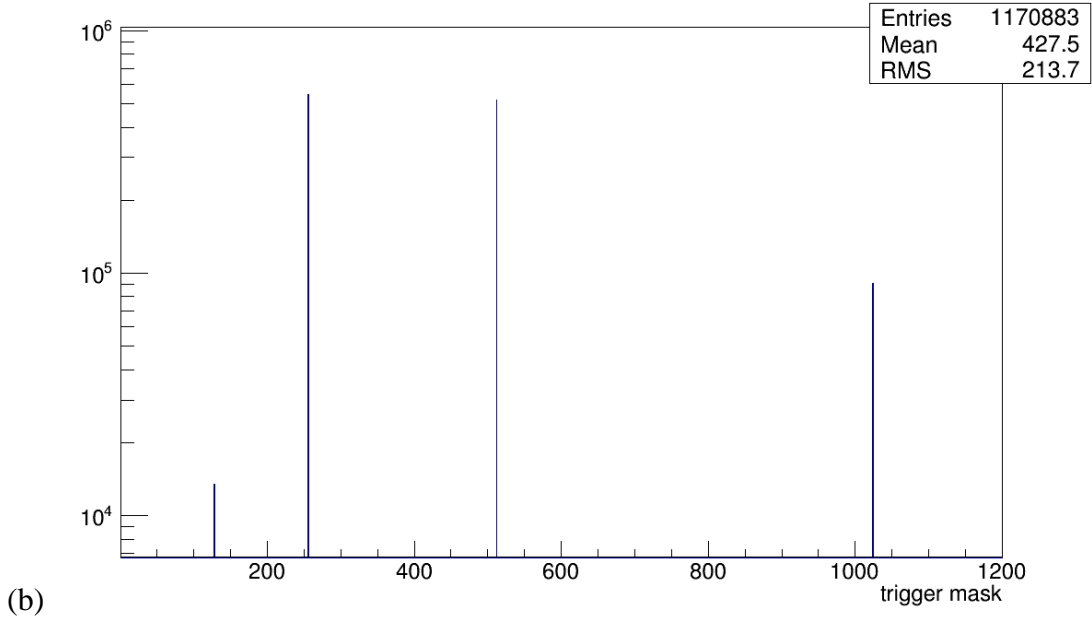
Figure 3.9: Trigger mask before the application of the cut (a) and right after it (b).

In figures 3.10 to 3.13 the kinematic distributions for dimuon pair are shown. On the figure 3.10, the dimuon momentum distribution is depicted for all masses (blue distribution) and also for masses larger than 2.5 GeV (red distribution). Next, the plot on the figure 3.11 shows the distribution of the Feynman's x variable (see Section 1.4). As the COMPASS is a fixed target experiment, the x_F is mainly positive, and for the high masses it peaks around 0.3 (see figure 3.11, [22]).
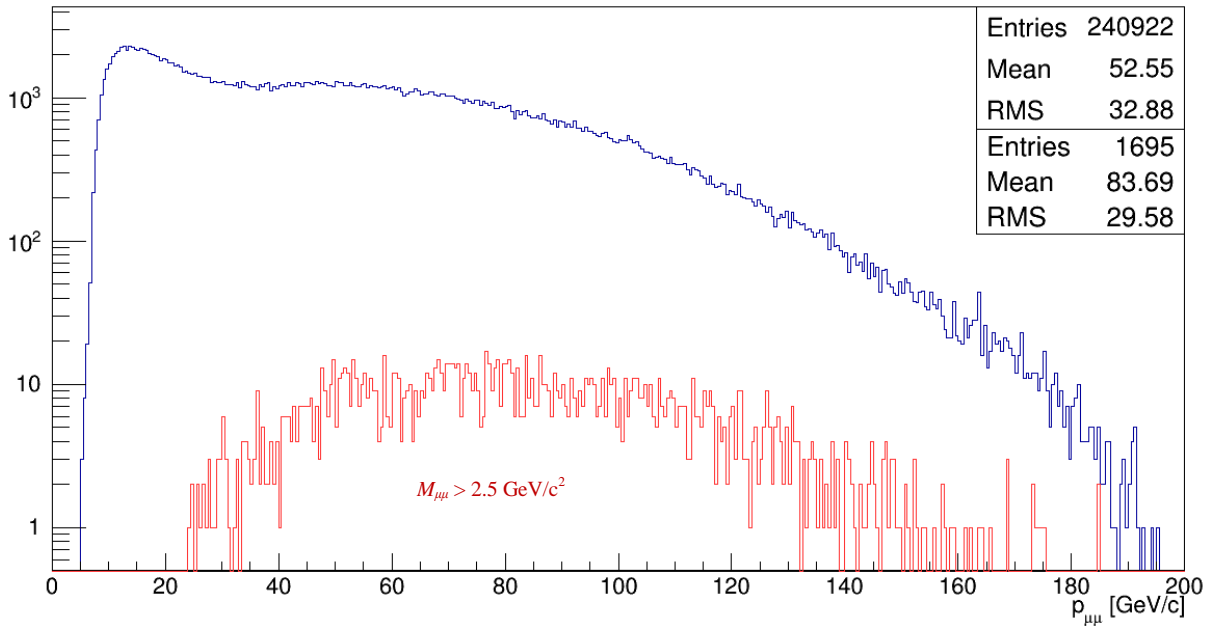
Figure 3.10: The dimuon momentum distribution, blue line denotes the distribution for all masses and red for masses larger than 2.5 GeV.
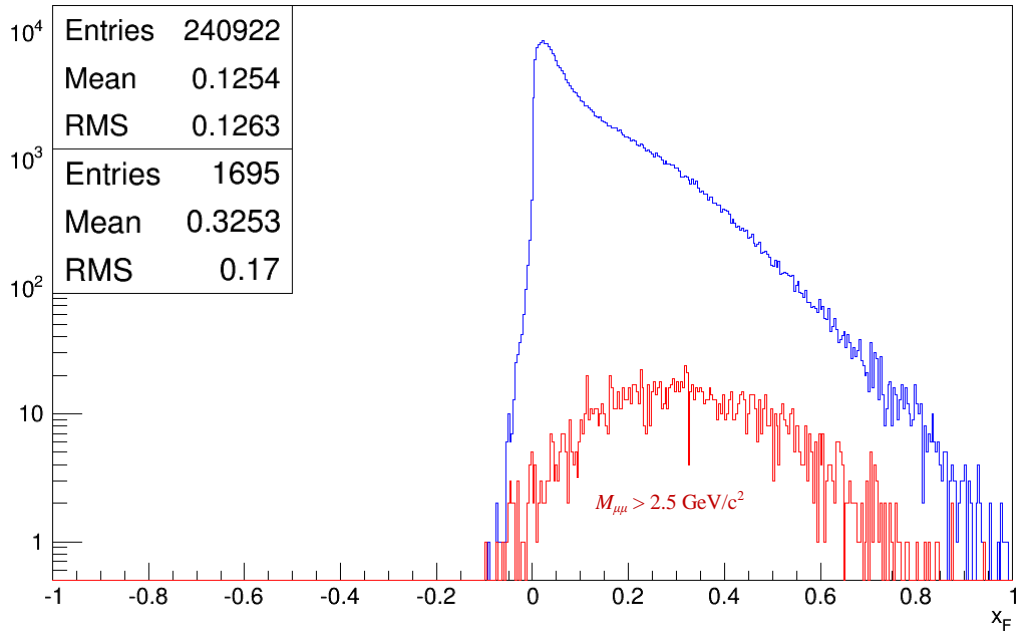
Figure 3.11: x_F variable for all masses (in blue) and higher than 2.5 GeV (in red).

Then, on the figure 3.12 the phase space coverage of x_1 versus x_2 for masses higher than 2.5 GeV is depicted (x_1 corresponds to x_π and x_2 corresponds to x_p from the theoretical section). There can be seen that the valence region of pion beam ($x_1 > 0.1$) dominates, while for the target nucleon there is a mixture of sea and valence regions [22]. The figure 3.13 shows the LAB angle between the two muons in degrees (after all selections).
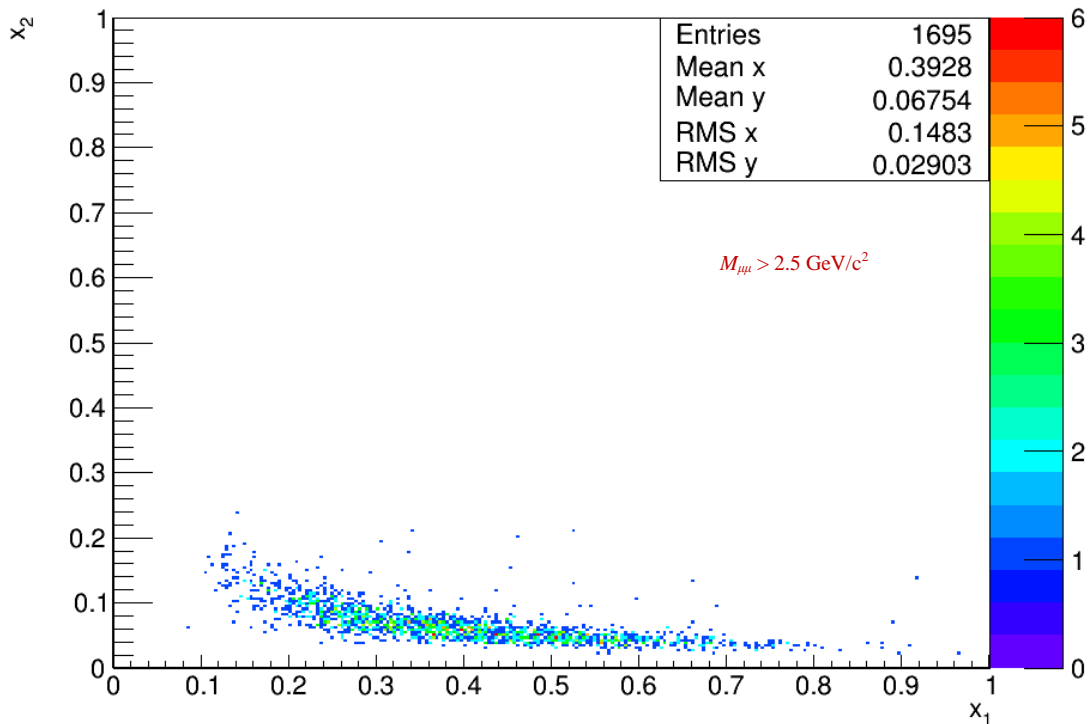
Figure 3.12: x_1 versus x_2 distribution for masses $M_{\mu\mu} > 2.5$ GeV.
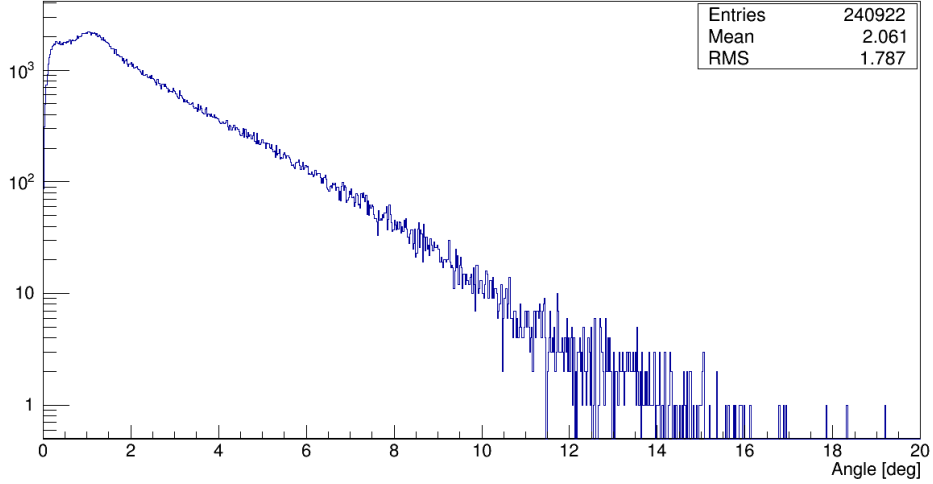
Figure 3.13: The angle between the momenta of muons (in LAB) after all cuts.

As can be seen from the figure 3.8, a very important part of the dimuon mass distribution in lower mass region is a combinational background. It is created by pairing of muons which came from a different interaction, i.e. uncorrelated muons. One of the combinational background sources are muons from pion secondary decay and kaon decay [22]. To evaluate this, we use the muon like-sign pairs (figure 3.14). According to [22], the distribution of the opposite sign pairs can be modeled as:

$$N_{\mu^+\mu^-}^{bg} = 2\sqrt{N_{\mu^+\mu^+}N_{\mu^-\mu^-}} \ . \tag{3.1}$$
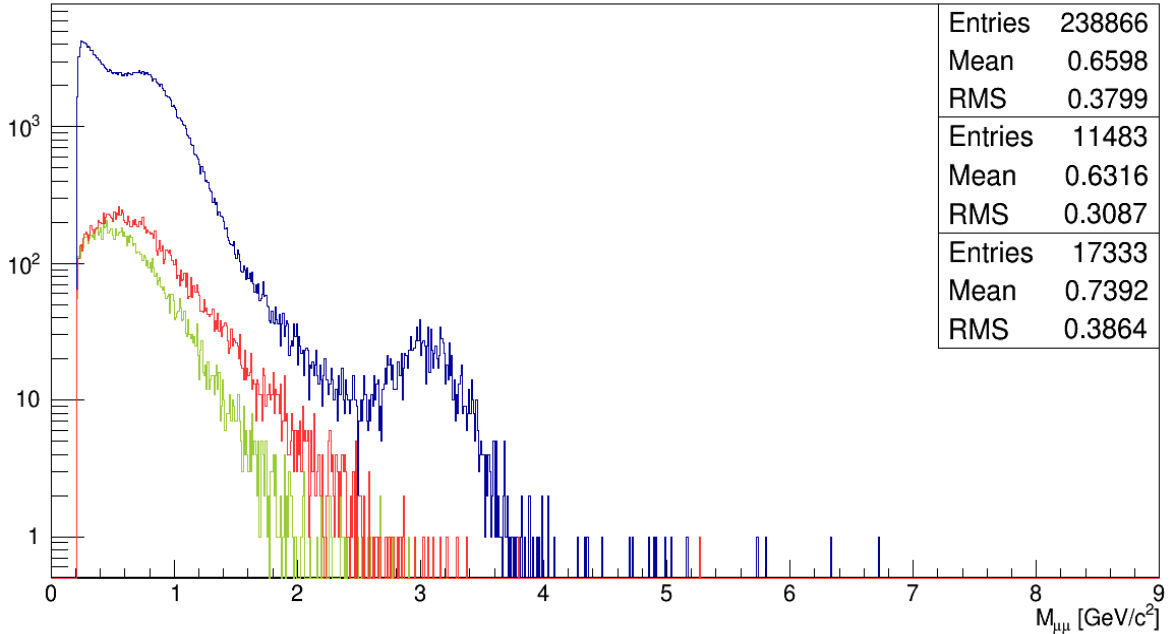
Figure 3.14: Mass distribution of the dimuon. In blue are the opposite sign muon pairs, in red are the negative like-sign pairs and in green are the positive like-sign pairs.

The figure 3.15 shows the combinational background (in green) fitted with the exponential function: $p_0 \cdot e^{p_1 \cdot M_{\mu\mu}}$. And the figure 3.16 shows final mass distribution after the image cut (made by subtracting of the histograms).
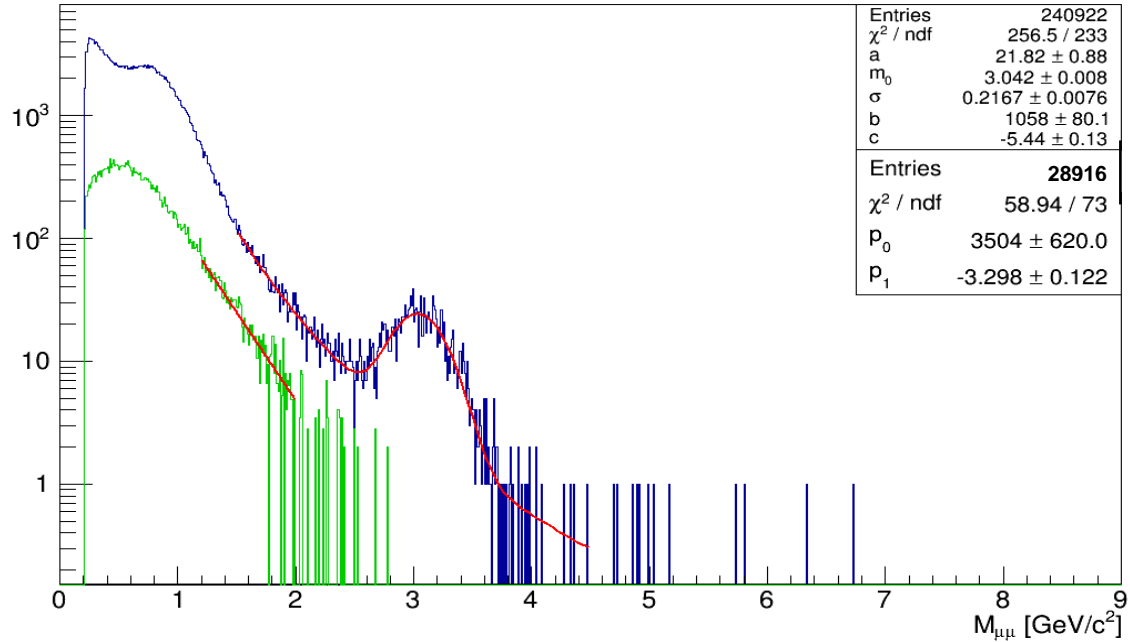

Figure 3.15: The fitted dimuon mass distribution (in blue) together with the fitted combinational background (in green).
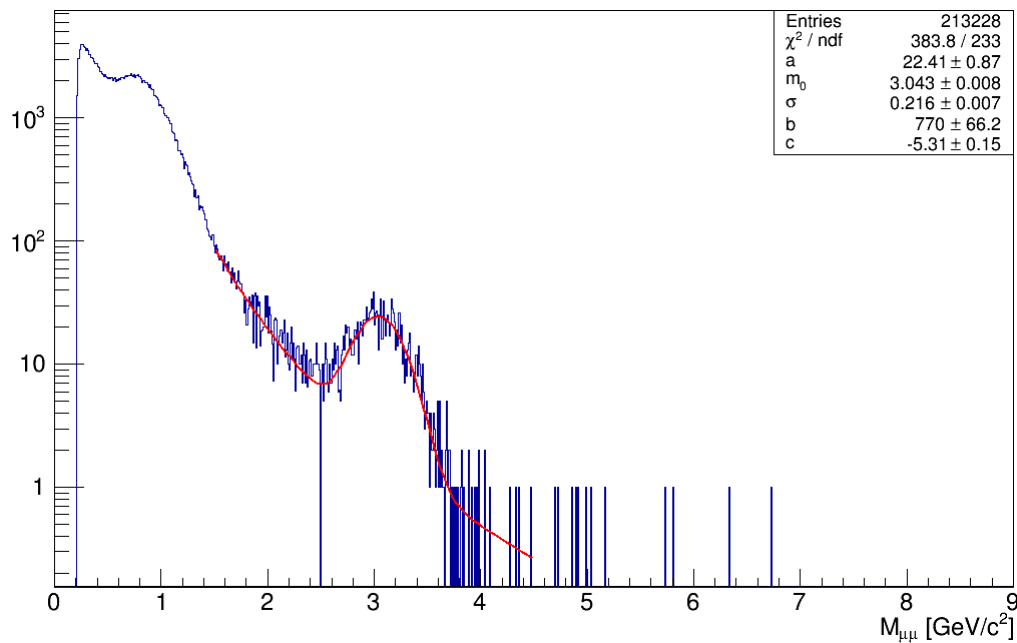

Figure 3.16: Dimuon mass distribution after the image cut.

The last figure, the 3.17, in this section shows the z distribution of all masses prior to any selection criterion while the region of the target (together with the margins; see selection

criterion 6) is indicated by the purple lines. One can see that downstream of the target, in the region of the hadron absorber, the production of the charged particles rises.
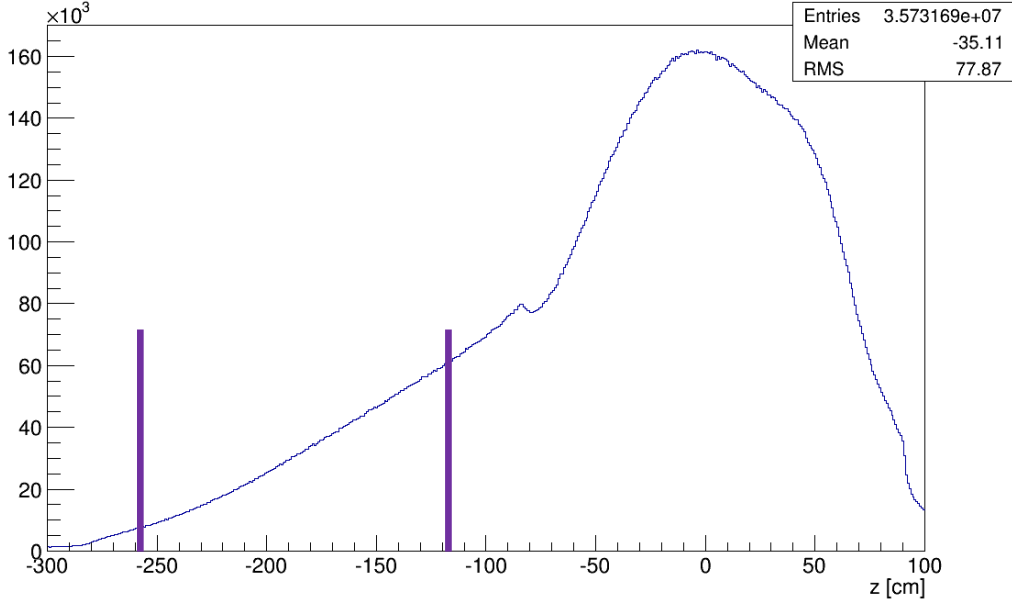

Figure 3.17: The distribution of all the charged particles along the *z* axis in the direction downstream of the target. The purple lines denote the borders of the target area.

For the comparison with the released results of the 2009 beam test and MC studies, see [22].

3.4 The analysis of the 2014 data taking

3.4.1 Data taking conditions

The 2014 DY pilot run began on 6th of October and lasted till the 15th of December in 2014. The run began with commissioning of the PT, PT magnet, detectors and triggers. On 26th of November a regular data taking started. The π^- beam of 190 GeV was used, the average intensity was 3.7×10^8 π^-/spill i.e. 8×10^7 π/s (the maximum intensity tested was 10×10^7 π^-/s) which was actually more than was proposed in [2] (see [24]). The size of the beam spot in the target was large: $\sigma \sim 1$ cm, in order not to heat up and depolarize the target material. Three periods of data taking were gathered: T5, T6 and T7 which consisted of 323 runs in total (36713 spills). The expected number of high mass dimuon of $M_{\mu\mu} > 4$ GeV was ~600 per day, with top limit ~900 per day [24].

The NH$_3$ 2-cell target was used. Unfortunately, only the unpolarized target had to be used because of the magnet was not fully operational. The length of each cell was 55 cm and

the diameter was 4 cm. The gap between the cells had 20 cm in length (see figure 2.6; for the photograph taken during loading the target material, see Attachment 3). The new hadron absorber (described in section 3.1) was constructed and positioned downstream of the target. Then, some detector modifications occurred. The Micromegas were replaced with improved Pixel Micromegas (see Attachment 4) positioned in front of the DC0 (see [24]). The triggers were optimized and the beam telescope underwent some modifications, e.g. the SciFi1.5 gained an additional detector plane (see Attachment 5). There was also a new detector added, namely the Vertex detector in order to improve the vertex reconstruction and cell separation of events.

3.4.2 The preliminary results of the 2014 data taking

The first production of data occurred in the beginning of 2015. The standard CORAL event reconstruction was performed. The total number of produced mDSTs was 3.796×10^9 [24]. We have used 260 runs consisting of 29310 spills (8.5×10^7 events) in our analysis. The selection criteria had to be modified in three following points: The target position has changed to $z = [-300, -150]$ (1st criterion), and of course so has the narrowed one from the 6th criterion $z = [-290, -160]$, and as the 7th criterion we use $Z_{last} > 1400$ cm. Other criteria are unchanged. The table 3.2 shows the list of the selection criteria and their impact on the statistics. The cleaning effect of the cuts on the statistics can be seen on the figure 3.18.

	Cut	# events		statistic [%]							
	microDST	84821650	100								
1.	Prim. vtx from the target region	27977740	33.0	100							
2.	$\mu^+\mu^-$ pair	12444160	14.7	44.5	100						
3.	Double trigger	12237120	14.4	43.7	98.3	100					
4.	$p_\mu < 100$ GeV	11278940	13.3	40.3	90.6	92.2	100				
5.	$-290 < Z_{vtx} < -160$ cm	9990381	11.8	35.7	80.3	81.6	88.6	100			
6.	$r_{vtx} < 1$ cm	4688780	5.5	16.8	37.7	38.3	41.6	46.9	100		
7.	$Z_{last} > 1400$ cm	1542838	1.8	5.5	12.4	12.6	13.7	15.4	32.9	100	
8.	$Z_{first} < 300$ cm	1516120	1.8	5.4	12.2	12.4	13.4	15.2	32.3	98.3

Table 3.2: The impact of each selection criterion on the statistics.
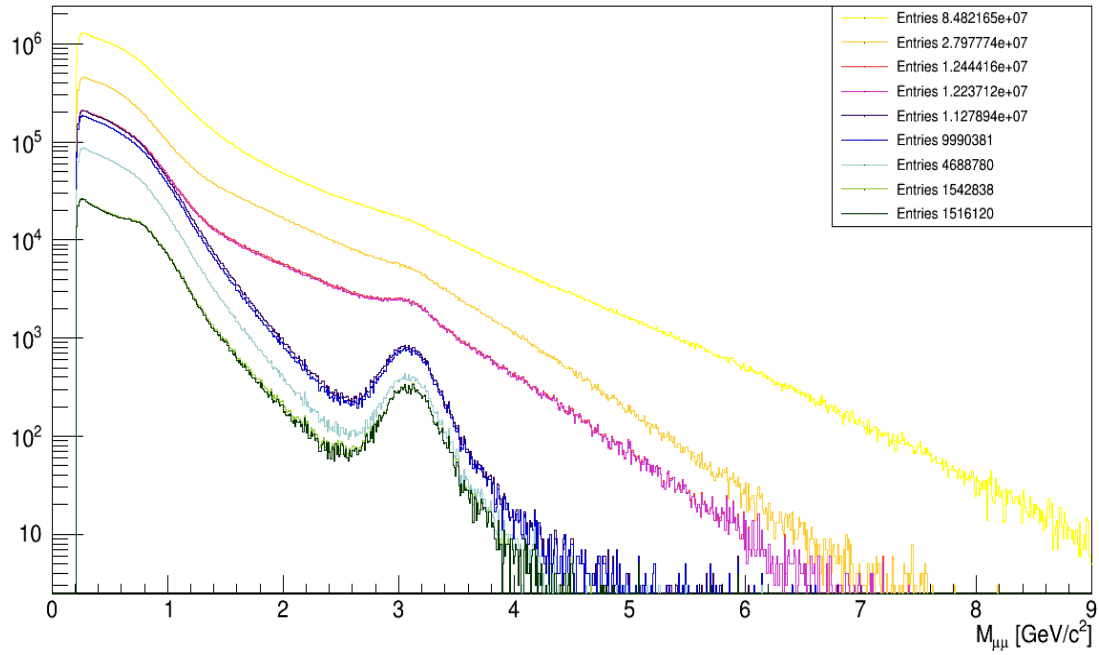
Figure 3.18: The impact of the selection criteria on the dimuon mass distribution.

(a)   (b)
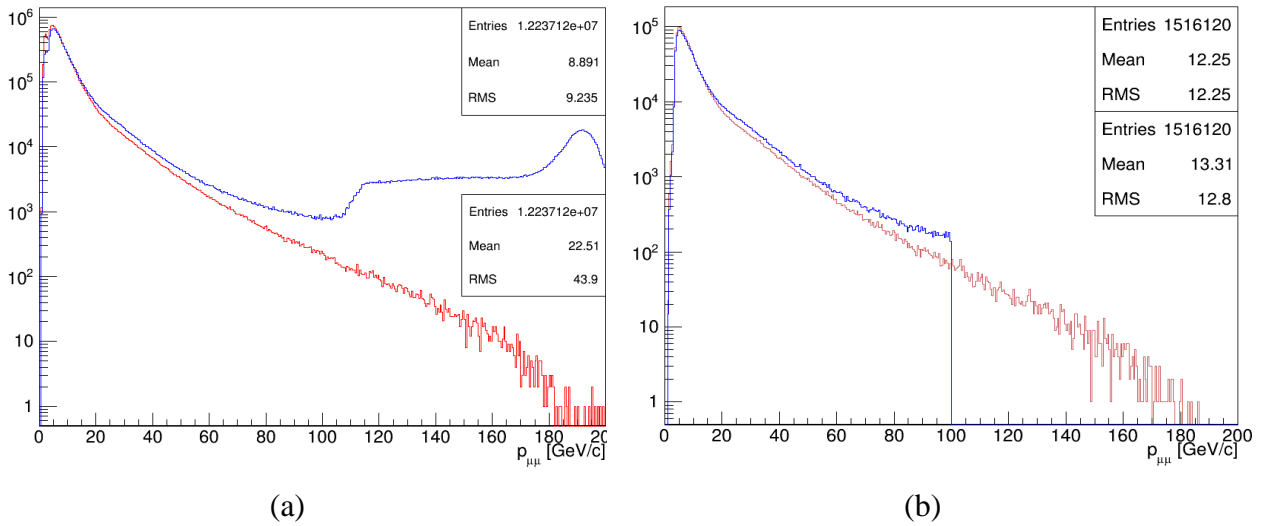
Figure 3.19: The kinematic distribution for μ^+ (in red) and for μ^- (in blue) before the cut (a) and after the cut (b).

The kinematic distribution of positive and negative muon is depicted on the figure 3.19. The figure 3.20 represents the comparison (a) between the Z_{vtx} distribution of all masses (in blue) and higher masses (in red). As one can see, the same result applies as for the 2009 data.

44

(a)

(b)
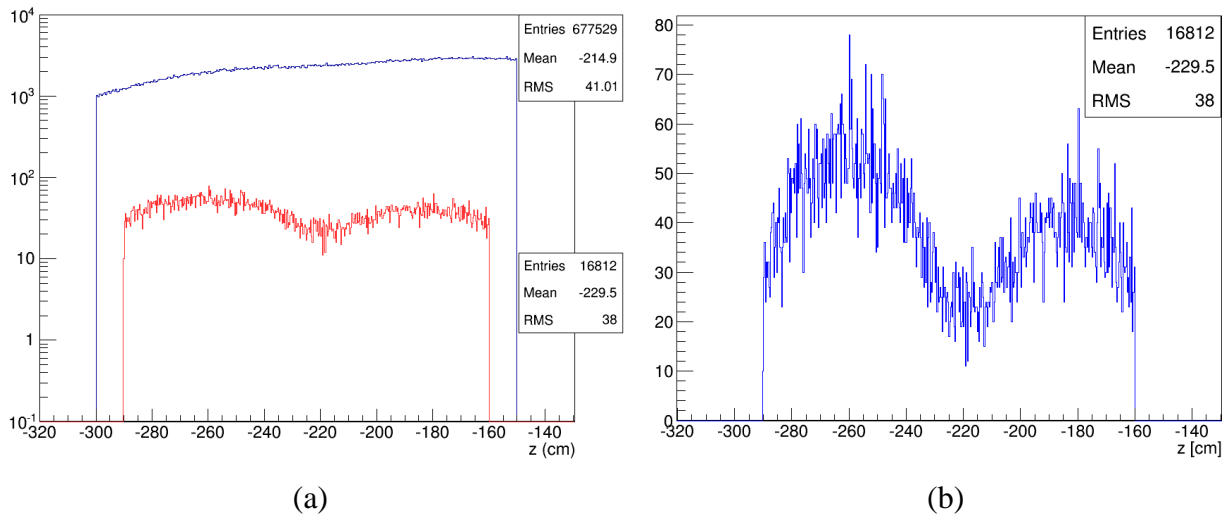
Figure 3.20: The comparison (a) between the Z_{vtx} distribution for all masses (in blue) and for $M_{inv} > 2.5$ GeV (in red). On (b) there is the high masses distribution only, in linear scale.


(a)

(b)
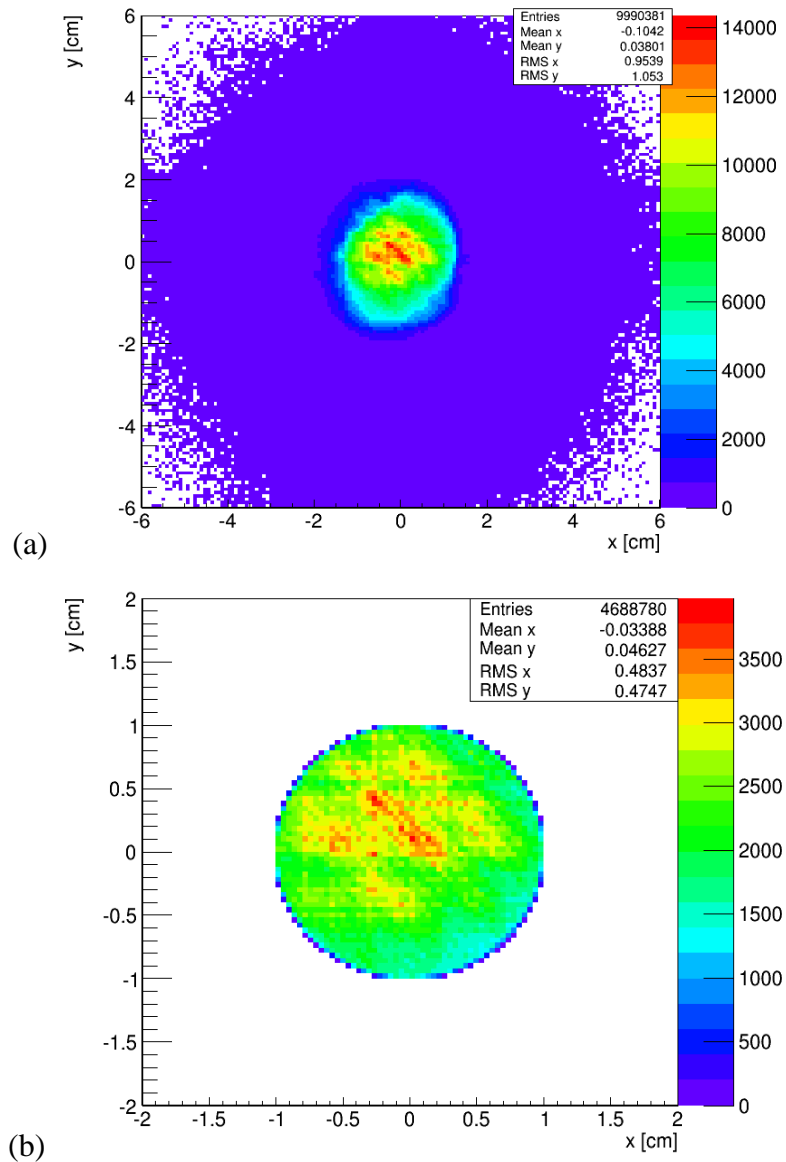
Figure 3.21: X_{vtx} versus Y_{vtx} profile of the beam (a) and the cut on 1 cm (b).

45

On the figure 3.21 (a) is visible that the beam profile is slightly flattened in *x* axis. The dimuon mass distribution after the selection cuts is shown on the figure 3.22. It can be seen that in this case the statistics is much better than in the 2009 analysis and the DY continuum is better populated due to that. And additionally, the ψ' peak is well visible (see figure 3.22). Hence, the fitting function is different; we used an equation as follows:

$$gaus(J/\psi) + b \cdot M^c_{\mu\mu} + gaus(\psi'). \qquad (3.2)$$

| χ^2 / ndf	393.6 / 317
a_1	284.7 ± 3.5
m_{01}	3.086 ± 0.002
σ_1	0.1952 ± 0.0023
b	8046 ± 174.2
c	-5.417 ± 0.036
a_2	10.77 ± 1.15
m_{02}	3.678 ± 0.025
σ_2	0.0961 ± 0.0168
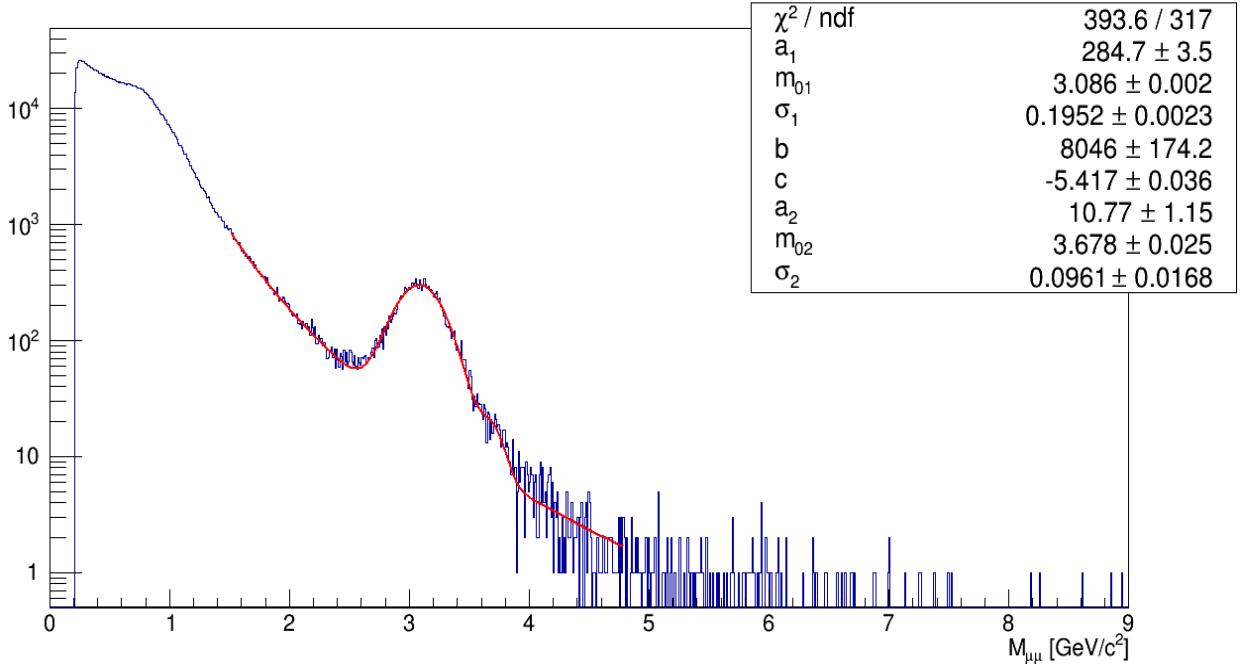
Figure 3.22: The dimuon mass distribution after all cuts with a J/ψ fit (parameters with subscript 1) and the ψ' fit (subscript 2) where a_1 and a_2 denote the amplitudes of the fits, m_{01} and m_{02} are the means i.e. the mass of the J/ψ and the ψ', respectively, and σ_1 and σ_2 describe the resolution of their mass regions.

The fitting range was extended to 1.5 to 4.8 GeV. After the integration, we get 13300 ± 130 J/ψ events with mass of 3.086 ± 0.002 GeV which is actually much more precise (see [26]) than in the test beam 2009 data, and a mass resolution of 195.2 ± 2.6 which is also better. The background processes of the J/ψ production is depicted on the figure 3.23.

In the DY 2014 run, a different set of triggers was used and so the trigger mask is different. The figure 3.24 (a) shows the distribution for the whole trigger set and the figure 3.25 the chosen trigger mask. This time, the logarithmic scale is used as the filling of the lower bits would not be visible in a linear scale. And on the (b) the selected trigger mask can be seen.
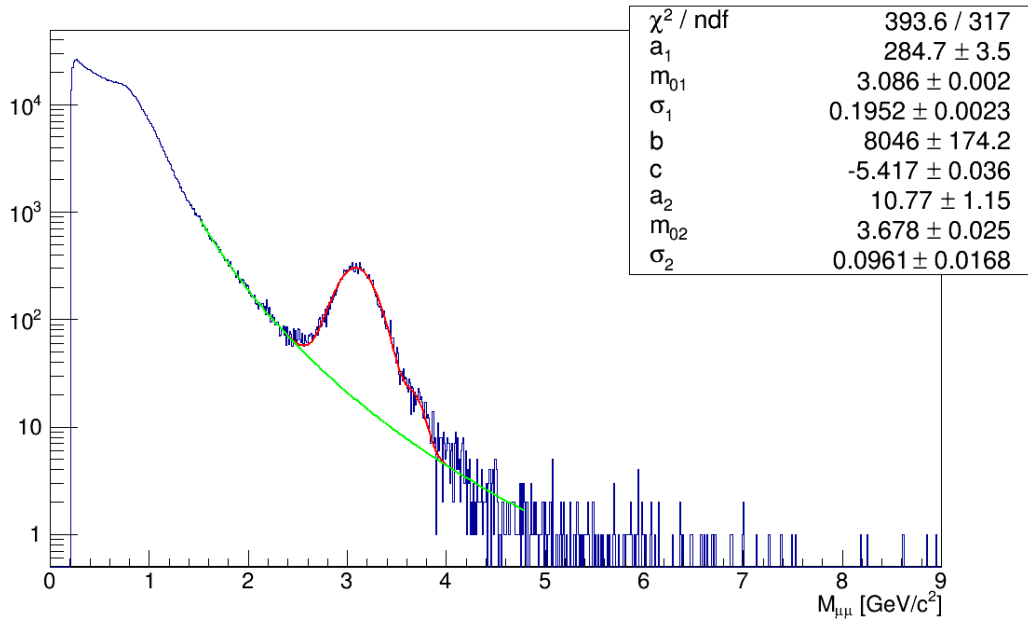
Figure 3.23: J/ψ fit (in red) and the background processes (in green).

(a)

(b)
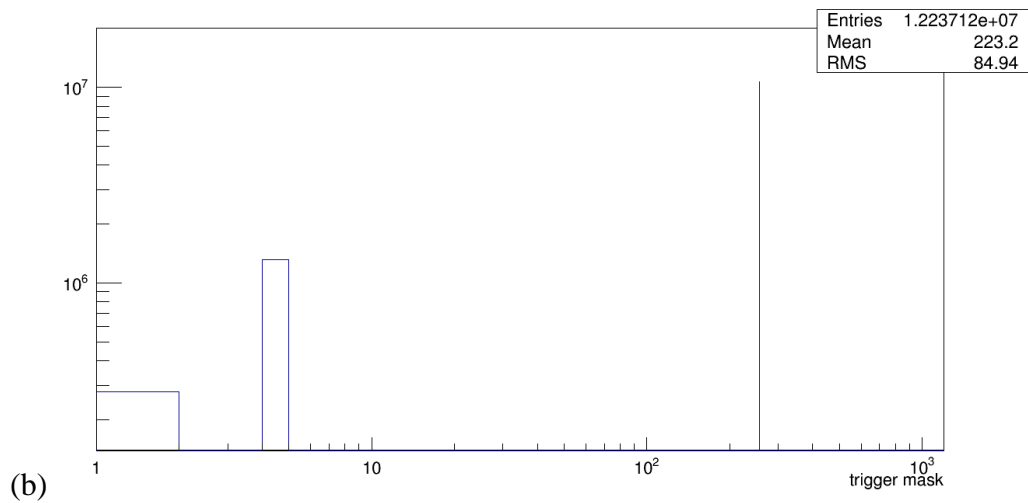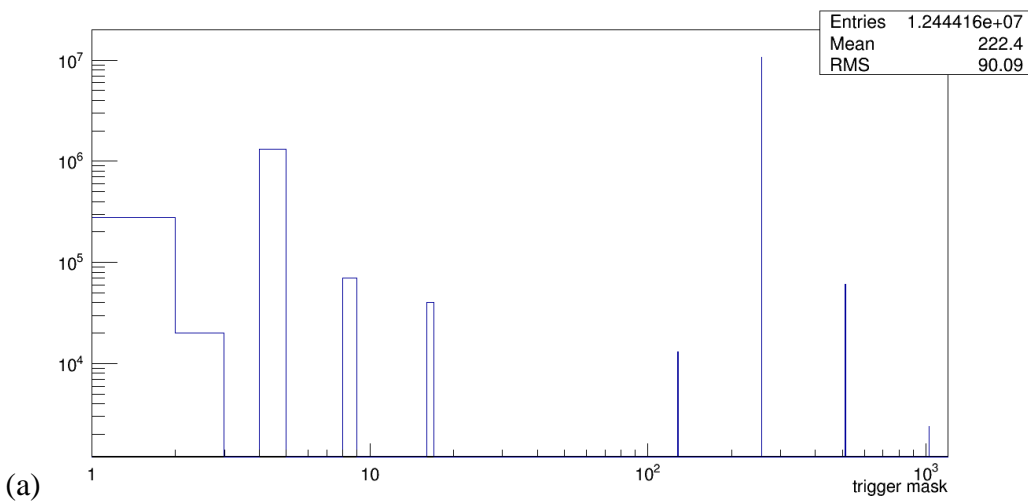
Figure 3.24: The trigger mask in logarithmic scale, before the cut (a) and after it (b).

The kinematic distributions of the muon pair are shown as follows. On the figure 3.25, the momentum distribution of the dimuon is shown for all masses (in blue) and for higher masses $M_{\mu\mu} > 2.5$ GeV (in red). Next histogram (3.26) shows the Feynman's x distribution for all the masses and for higher masses (colors stay the same). The phase space of the x_1 versus x_2 is on the figure 3.27. The same what has been stated in the section 3.3 applies here as well, and higher statistics confirms that. It also satisfies the expectations (see [2]).
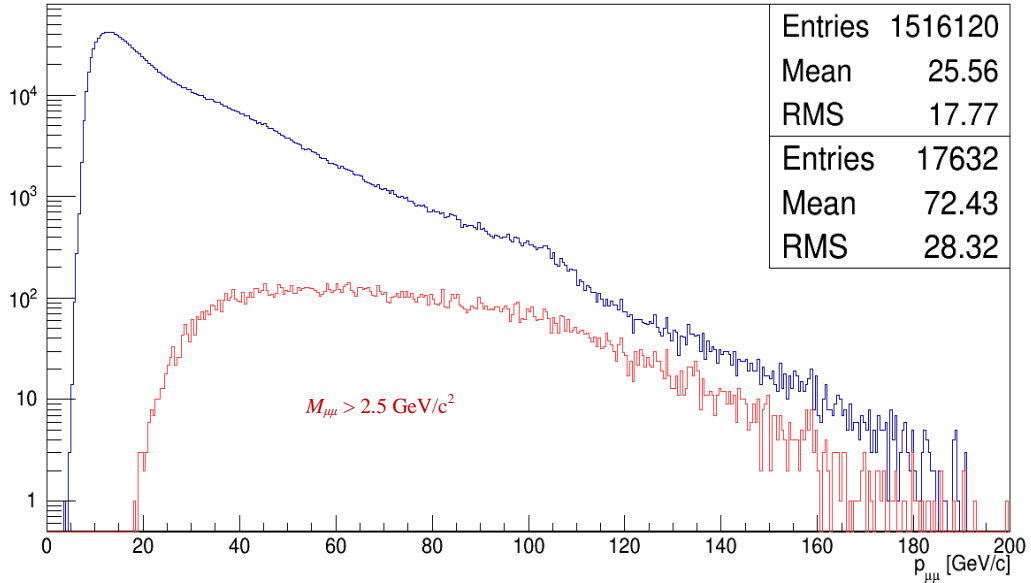

Figure 3.25: The dimuon momentum distribution for all masses (in blue) and for higher masses (in red).
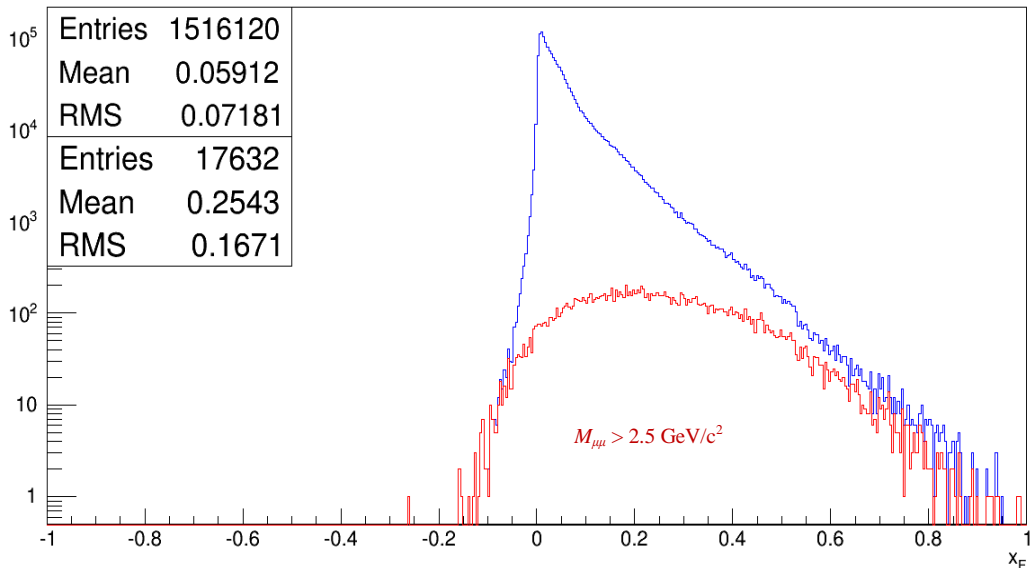

Figure 3.26: The x_F distribution for all masses (in blue) and for $M_{\mu\mu} > 2.5$ GeV (in red).

48
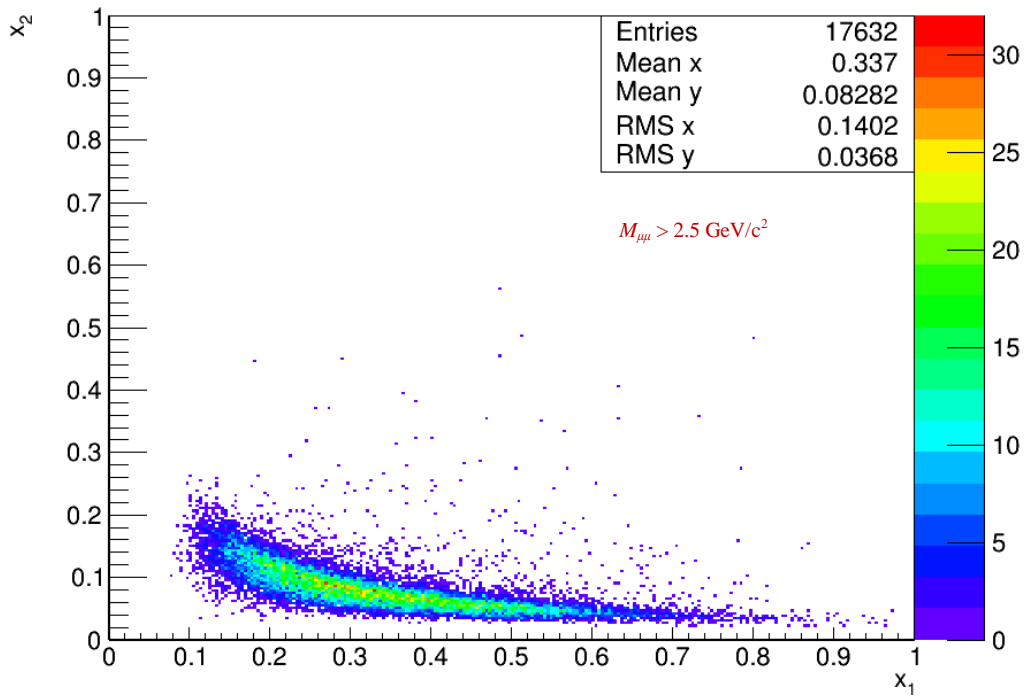
Figure 3.27: x_1 versus x_2 phase space distribution for higher masses.

The last two figures show the angle between the momenta of the two muons from the events after all the selections (figure 3.28) and the distribution of all the unselected events along the z axis showing the target area and the region downstream of it (figure 3.29). And as before, the purple lines demarcate the target area.
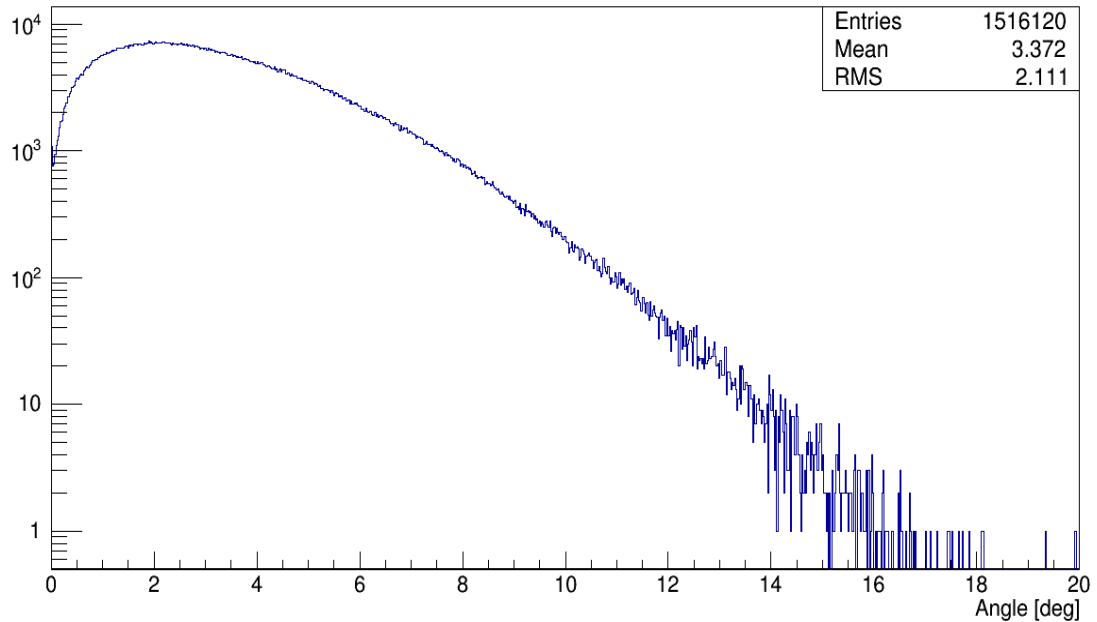

Figure 3.28: The distribution of the angle between the muons from the dimuon pair in degrees.
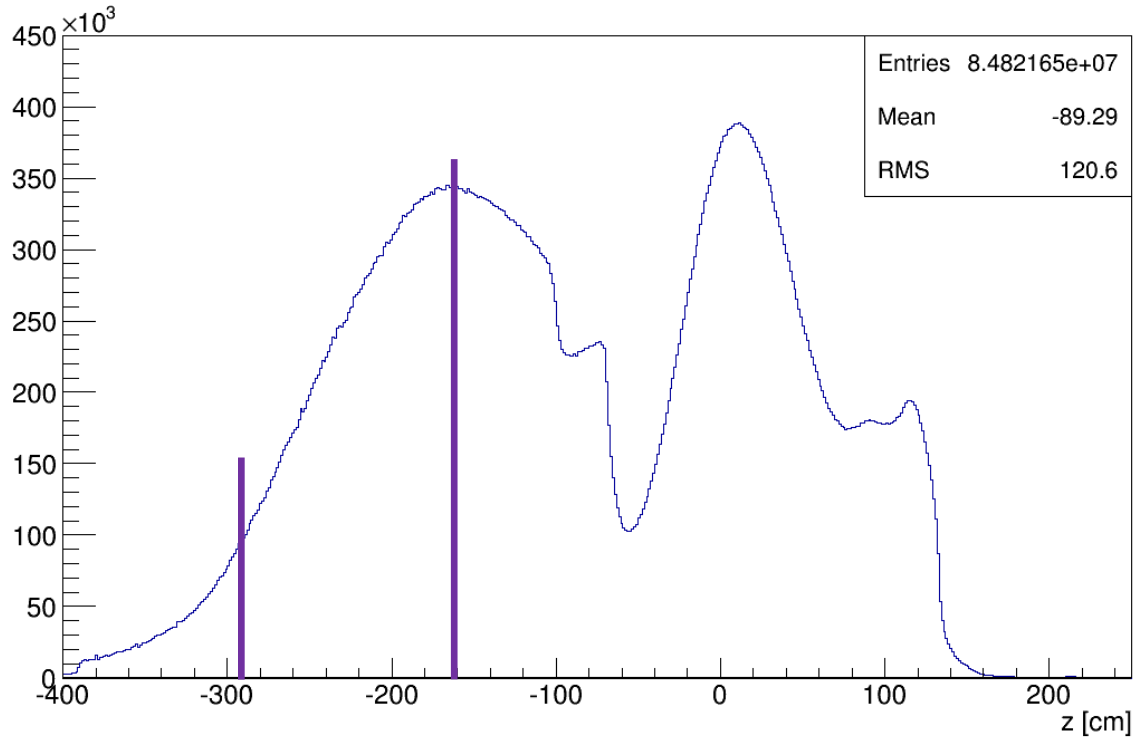
Figure 3.29: The distribution of all the unfiltered masses along the *z* axis. The purple lines denote the borders of the target.

It can be seen, that the results correspond with the ones from the 2009 beam test (see section 3.3), and also with the official results presented (see [25]).

3.5 Expectations of the DY 2015 program

The DY pilot run in the 2014 was the final preparation for the 2015 DY run which takes place in present days. The 2015 run started on the 27th of April and its conclusion is planned to 15th of November this fall. The original assumption in the COMPASS Proposal II [2] was to have two years of measurement with the intensity of 6×10^7 π^-/s and 48 s lasting SPS supercycle. But the plans have changed to have 180-days-lasting measurement only because of the shorter supercycle (33.6 s) and higher intensity of 10×10^7 π^-/s. The expected counting rate of $M_{\mu\mu} > 4$ GeV events was 809 events per day (in proposal, [2]) and rescaled on the higher intensity, 2000 events per day. Nowadays, it seems we will have 140 days of measurement with the high intensity beam at our disposal. However, during the 2014 DY pilot run some difficulties appeared. Two factors haven't been taken into account, namely the Veto dead time and the μ identification efficiency which were measured in 2014, being 27% and (82 ± 4)%, respectively [24]. Due to those factors the expectations had to be

rescaled ones again to 980 events per day with present intensity. Thus, there is an agreement with the original expectation in order of magnitude. The final expectation of the number of high mass DY events from the whole run can be estimated as ~137000. Both the Veto dead time and the μ identification efficiency can probably be improved, so in fact we may get even closer to the original expectations.

Concerning the hardware changes, the target polarization is presently at operation. The target material loading occurred on 9th of April 2015 and the beginning of the polarization procedure took place in the beginning of May. The expected level of the polarization is 90% and the dilution factor about 0.22. Another change is the addition of DC05 detector (for the photographs of the preparation works and DC05 detector, see Attachments 6 and 7, respectively) which occurred on 12th of May. The purpose of the additional detector was to replace the Straw2 detector which became outdated and inefficient. The RICH detector will be filled with nitrogen in the present arrangement. However, it has a low priority in DY run because it is not needed for the identification of muons. Besides those major changes, some minor modifications are in place on the spectrometer. The Attachment 8 shows some additional works during the installation of the DC05; description below.

Conclusion

In the presented thesis, the basic physics principles of Drell-Yan polarized process were introduced. The deep inelastic scattering and its observables were described for comparison. We briefly discussed the contemporary state of the art of the nucleon spin structure studies. The nucleon structure functions (PDFs and TMDs) were outlined together with the way to access them via the spin asymmetries. The main goals of the Drell-Yan program at COMPASS were presented. The results of this experimental program are going to be a very important verification of the QCD in a non-perturbative regime and may contribute notably to the solution of the spin puzzle, together with other COMPASS experimental programs.

The description of the COMPASS spectrometer was given and the importance of the transversely polarized target was demonstrated. Also the choice of material for the polarized target was mentioned. The basic features of the new DAQ system were presented. We summarized the modifications of the apparatus needed for the DY program. The most important one is the polarized target already mentioned and the hadron absorber. The hadron absorber will be needed for lowering the occupancies of trackers by the beam hadrons and the secondary (or tertiary) hadrons and electrons, which are not needed in the measurement of DY process. The essential role of the Monte Carlo simulation programs in high energy particle physics was shown and the specific MC code COMGEANT used at COMPASS was briefly introduced.

The two periods of data taking were described and analysed. The first was the 2009 DY beam test, a three-days-lasting program, where the configuration for the DY measurement has been tuned. And the second, the 2014 DY pilot run which was the preparation for the about half-a-year long 2015 DY data-taking that is going on presently. It has been shown that the 2009 beam test has been a successful preparation for the DY program as it fulfilled the expectations outlined in the COMPASS proposal II [2]. The results of the 2009 analysis correspond with the ones obtained from the official analysis and the MC studies performed [22]. In the 2014 data analysis almost the same procedure was applied in order to make a comparison (for the necessary exceptions, see section 3.4.2). The results agree with the ones obtained from the 2009 analysis and even the official results [25]. However, one of the selection criteria used in the 2014 analysis was apparently inaccurate. As can be seen in the

figure 3.21, the cut of the beam diameter to 1 cm (selection criterion no. 6) was too severe. The beam in 2014 was wider in diameter then in 2009, thus the cut should have been wider as well to cut off only the halo. Hence, the statistics has been unnecessarily deprived of useful data. As can be seen on the figure 3.18, after the 6th selection criterion when the statistics dropped from 9990381 events to 4688780 (the light blue line), the resolution of the higher mass region ($M_{\mu\mu} > 2.5$ GeV) hasn't improved, but the whole statistics lowered deeply. By this cut, we might have lost a great part of statistics. Nevertheless, the other cuts seem to have been applied properly and the outcome approves the former analysis.

Bibliography

[1] Ashman, J. et al.: An Investigation of the Spin Structure of the Proton in Deep Inelastic Scattering of Polarized Muons on Polarized Protons, Nucl. Phys. B328, 1-35, 1989.

[2] Gautheron, F. et al.: COMPASS-II Proposal, 2010, CERN-SPSC-2010-014,SPSC-P-340.

[3] Williams, W. S. C.: Nuclear and Particle Physics, Oxford University Press, 1991.

[4] Chýla, J.: Quarks, partons and Quantum Chromodynamics, Praha, 2004, available at: http://www-ucjf.troja.mff.cuni.cz/new/wp-content/uploads/2014/02/text.pdf.

[5] Matoušek, J.: Studies of Drell-Yan process at Compass experiment, Diploma thesis Charles University, Prague, 2013, available at: http://wwwcompass.cern.ch/compass/publications/welcome.html#theses.

[6] Devenish, D., Cooper, A.: Deep Inelastic Scattering, Oxford University Press, 2011.

[7] Pešek, M.: Low temperature proton polarized target for nucleon structure studies at COMPASS, Diploma Thesis, Charles University, Prague, 2014, available at: http://wwwcompass.cern.ch/compass/publications/welcome.html#theses.

[8] Bjorken, J.D., Paschos, E. A.: Phys. Rev. 185 (1969), 1975.

[9] Le Goff, J.-M.: The Spin structure of the nucleon, Habilitation Thesis, Universite de Paris-Sud U.F.R. Scientifique D'Orsay, Paris, 2005, available at: http://wwwcompass.cern.ch/compass/publications/welcome.html#theses.

[10] Alekseev, M. et al.: Phys. Lett. B 693 (2010), 227-235.

[11] Arnold, S., Metz, A., Schlegel, M.: Phys. Rev. D 79 (2009), 034005.

[12] Drell, S. D., Yan, T. M.: Phys. Rev. Lett. 25 (1970), 316.

[13] Abbon, P. et al.: The COMPASS experiment at CERN, NIMA 577, 455-518, 2007.

[14] Abbon, P. et al.: The COMPASS setup for Physics with Hadron Beams, NIMA 779, 69, 2014.

[15] Kondo, K. et al.: Polarization measurement in the COMPASS polarized target, NIMA 526, 70-75, 2004.

[16] Doshita N. et al.: Performance of the COMPASS polarized target dilution refrigerator, NIMA 526 (2004), 138-143.

[17] Nový, J.: COMPASS DAQ – Basic control system, Diploma Thesis, CTU, Prague, 2012.

[18] Nový, J.: Personal communication.

[19] Bodlak, M. et al.: New data acquisition system for the COMPASS experiment, Journal of Instrumentation, 2013-02-01, vol. 8, issue 02, DOI: 10.1088/1748-0221/8/02/C02009, available at: http://iopscience.iop.org/1748-0221/8/02/C02009/.

[20] Denisov, O.: 2012 Drell-Yan test beam – proposal, expectations, results. Presented on Drell-Yan Analysis meeting, CERN, February 4, 2013.

[21] Denisov, O. et al.: COMPASS Note 2010-05, CERN, 2010, available at: http://wwwcompass.cern.ch/compass/notes/2010-5/2010-5.pdf.

[22] Quaresma, M. et al.: COMPASS Note 2013-11, CERN, 2013, available at: http://wwwcompass.cern.ch/compass/notes/2013-11/2013-11.pdf.

[23] Quaresma, M.: 2009 DY beam test 3rd production analysis – J/ψ shift. Presented on Drell-Yan Analysis meeting, CERN, January 31, 2014.

[24] Denisov, O.: Status of the 2014 pilot DY run and preparations for 2015. Presented on the COMPASS Collaboration meeting, CERN, December 4, 2014.

[25] Quaresma, M.: 2014 data analysis. Presented on Drell-Yan Analysis meeting, CERN, May 13, 2014.

[26] PDG live, J/ψ meson, available at: http://pdg8.lbl.gov/rpp2014v1/pdgLive/Particle.action?node=M070.

[27] Riedl, C.: DC5 - Status of Construction. Presented on Drell-Yan Hardware meeting, CERN, November 20, 2013.

List of Abbreviations

CASTOR   CERN Advanced STORage manager

CEDAR   Cherenkov Differential counter with Achromatic Ring focus

CERN   European Organization for Nuclear Research (originating from 'Conseil Européen pour la Recherche Nucléaire')

CMS   Center-of-Mass System

COMPASS   Common Muon and Proton Apparatus for Structure and Spectroscopy

CORAL   COmpass Reconstruction and AnaLysis

CS   Collins-Soper frame

DAQ   Data Acquisition System

DC   Drift Chamber

DIS   Deep inelastic scattering

DNP   Dynamic Nuclear Polarization

DR   Dilution Refrigerator

ECAL(1,2) Electromagnetic calorimeter (1 or 2)

EMC   European Muon Collaboration

HCAL(1,2) Hadronic Calorimeter (1 or 2)

LAS   Large Angle Spectrometer

LO QCD   Leading-Order Quantum ChromoDynamics

MC   Monte Carlo method

mDST   mini Data Summary Trees

μDST   micro Data Summary Trees

MW(1,2)   Muon Wall (1 or 2)

MWPC   Multiwire Propotional Chamber

NMR   Nuclear Magnetic Resonance

PT   Polarized Target

|	
QCD	Quantum Chromodynamics
QED	Quantum Electrodynamics
QM	Quark Model
PHAST	PHysics Analysis Software Tool
RICH	Ring Imaging Cherenkov detector
SAS	Small Angle Spectrometer
SciFi	Scintilating Fibers
SIDIS	Semi-inclusive deep inelastic scattering
SLAC	Standford Linear Accelerator
SPS	Super Proton Synchrotron
TF	Target rest Frame

Attachment
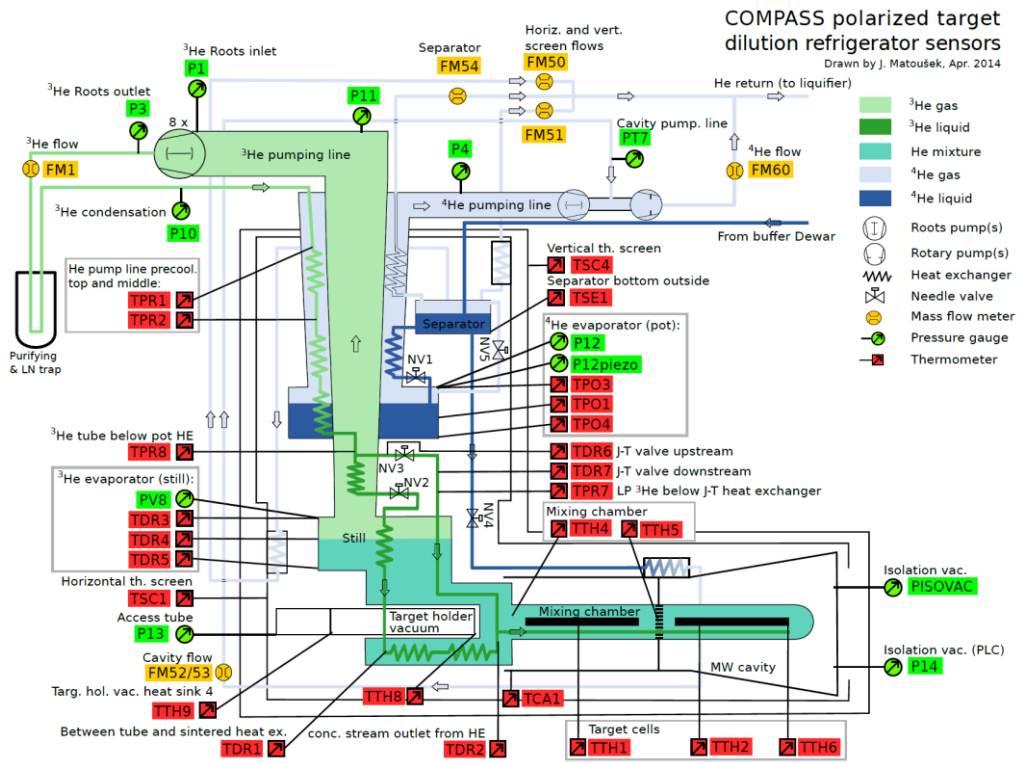
Attachment 1: The detailed scheme of the PT dilution refrigerator.
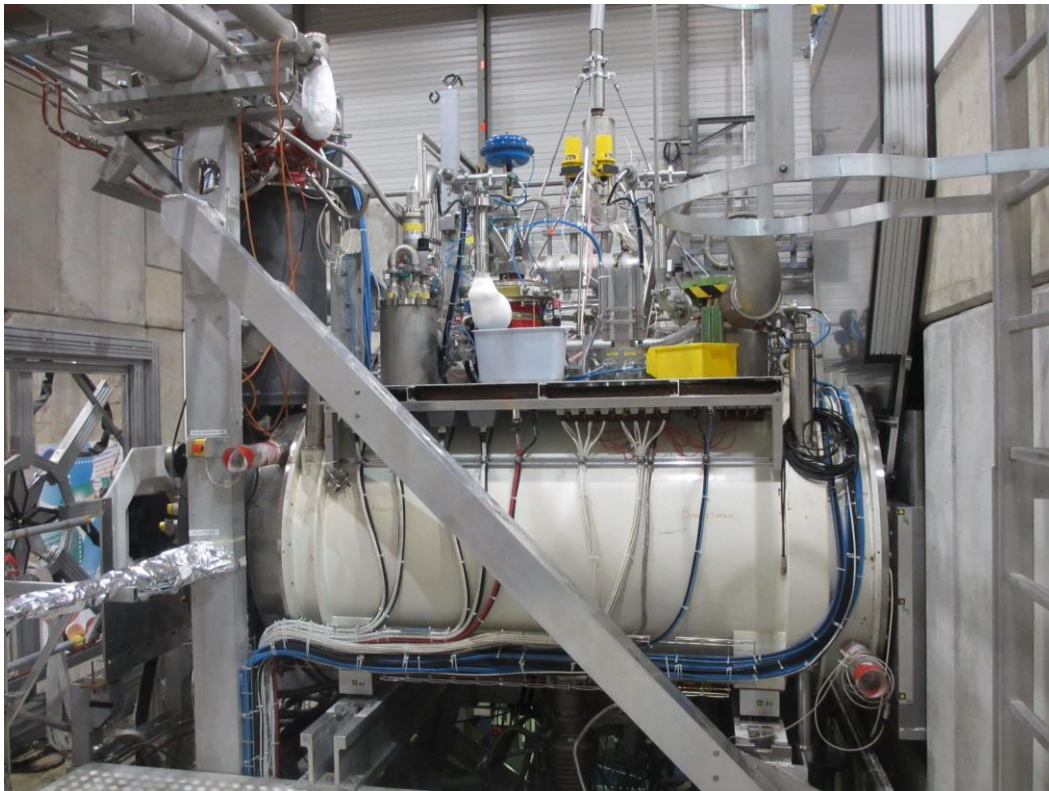
Attachment 2: The polarized target. The vertical black tube on left contains the main part of the dilution refrigerator.

Attachment 3: The target material loading (from [24]).
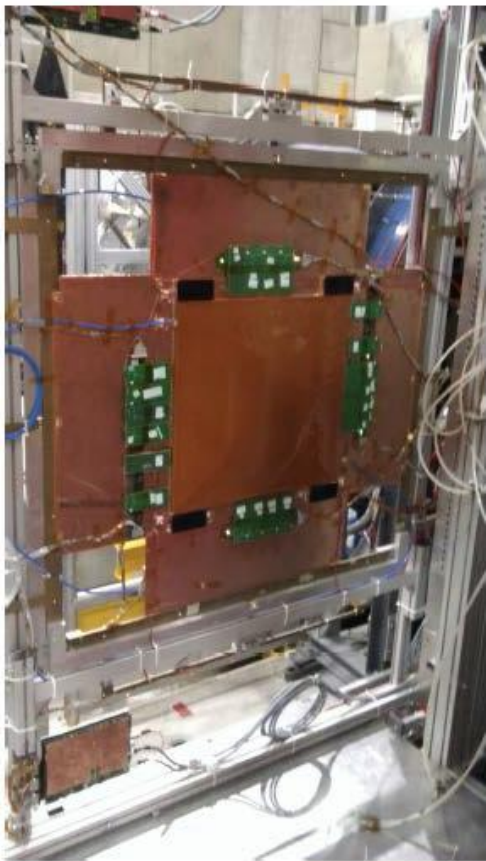

Attachment 4: The Pixel MicroMegas [24].

Attachment 5: The photograph of the beam telescope consisting of the VETOinner1 (first left), SciFi1.5 (middle), VETOinner2 (the next plane, on the right), and the SciFi3 (the very right).

Attachment 6: The preparations for the installation of the DC05 detector. The detector DC04 is moved out to the garage position. Vertically across the center of the detector the GEM detector is placed (left picture).
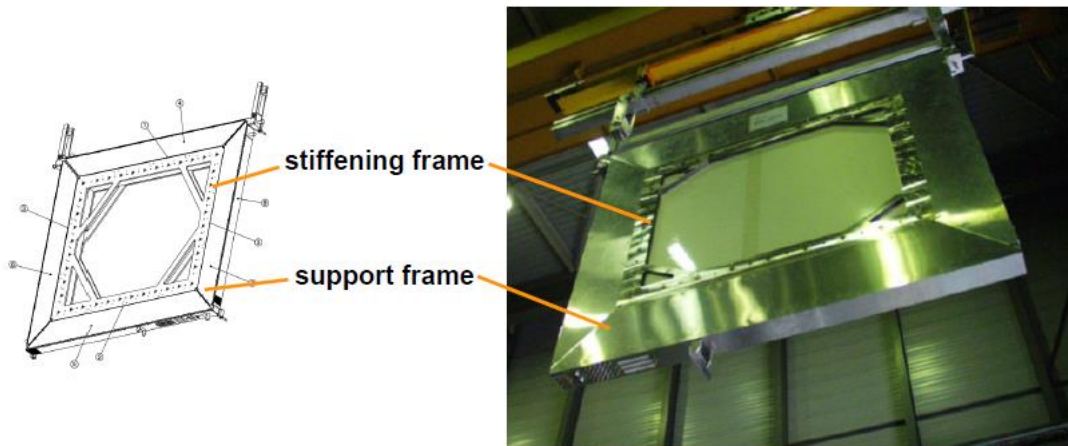
Attachment 7: The new DC05 detector (from [27]).
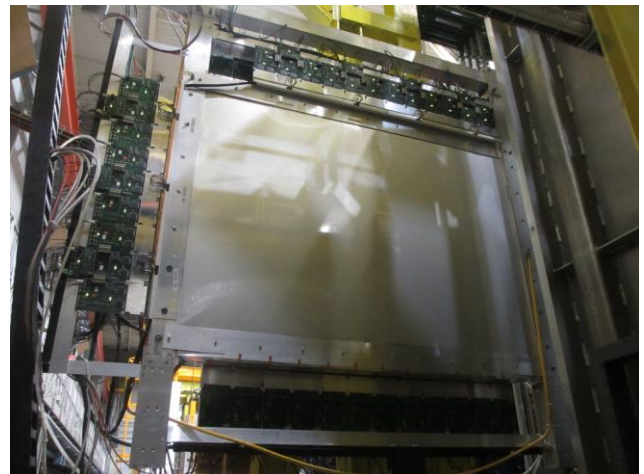
Attachment 8: The works on the installation of the DC05. The left upper figure shows the DC04 in the garage position from upstream side. On the right upper, the Straw3 is being moved out to the garage position beside the DC04. The left bottom in the Straw3 already parked and the right bottom shows the MWPC PS01 detector also in the parking position. Also, there was some tuning of these detectors performed because of the noise they made.